

CHARACTERIZATION OF PULSE-SHAPE
DISCRIMINATION FOR BACKGROUND REDUCTION IN
THE DEAP-1 DETECTOR

by

PARADORN PASUTHIP

A thesis submitted to the
Department of Physics, Engineering Physics and Astronomy
in conformity with the requirements for
the degree of Master of Science (Engineering)

Queen's University
Kingston, Ontario, Canada

January 2009

Copyright © Paradorn Pasuthip, 2009

Abstract

DEAP (Dark Matter Experiment with Argon and Pulse Shape Discrimination) is an experiment that aims to directly detect dark matter particles via nuclear recoils in liquid argon. The experiment uses the scintillation property of liquid argon as a means to discriminate the γ and β backgrounds from the expected signal. DEAP-1 is a 7 kg single phase liquid argon detector. It was constructed to demonstrate the scalability for a larger (3600 kg) detector. The detector was originally operated at Queen's University, where the background rejection level achieved was 6.3×10^{-8} for the recoil detection efficiency of 97.1%. The detector was relocated to SNOLAB, where the background in the energy region of interest was reduced by a factor of 7.7 (from 4.61 ± 0.17 mHz to 0.60 ± 0.05 mHz.). The background rejection level of 9.64×10^{-9} (10.4 part per billion) was achieved from the combined data set (Queen's University and SNOLAB) for a recoil detection efficiency of 35.5 ± 1.3 %. With the current background rate, the background rejection level required for the 3600 kg detector (1.8×10^{-9}) is projected to be achieved in 382 days at the neutron efficiency of 9.1 ± 0.6 %.

Acknowledgement

First of all, I would like to thank my supervisor, Mark Boulay, for his support and encouragement, for his superhuman ability to cope with my stupidity, for allowing me to work with such a wonderful experiment, and last but not least, for reading and correcting my thesis semi-infinite times.

I would like to express my gratitude to people who make my work possible and enjoyable: Bei Cai for reading and correcting my thesis, and for all her help with the data analysis. Chris Jillings for reading my thesis and all the help at SNOLAB. Jeff Lidgard for his pioneering thesis, for convincing me to join DEAP, and for all the water boxes. Aksel Hallin for accepting me as a graduate student and for introducing me to programming and experimental physics. Ryan MacLellan for all his help with codings, and for cleaning my house. Peter Skensved for his help with electronics, and for teaching me how to get rid of students. Jason Visser for CS and SC. Alex Wright for answering many of my silly physics questions and for being such an awesome officemate. Victor Golovko for all the help with the Monte Carlo. Art McDonald for his kindness and generosity. My middle school science teacher, Achara Ongsiriwittaya, for being such a great science teacher. Wolfgang Rau for answering all my physics questions. Hugh Evans and Hamish Leslie for their help with the annulus. Tony Noble and Mark Chen whose talks had sparked my interest in particle physics. Barry

Roberson for finding me an office. Anna Davour for teaching me about crazy cultures and steampunk, and for letting her daughter be my friend. Tina Pollman for all the cookies. Ryan Martin for his help with various things. All the students in Stirling 154 for allowing me to waste our time with many little chats. My self-proclaimed “great friend” and ex-housemate, Ryan Yee, because he said he deserved to be acknowledged.

I would like to thank David Bearse, Maizie Dafoe, Fraser Duncan, Chuck Hearn, Noel Gagnon, Rob Gagnon, Steve Gillian, Ian Lawson and all the DEAP summer students who have been very helpful with my work. For all the people in the particle physics group whose companionship had made my time at Queen’s University enjoyable; Berta Beltran, Ken Clark, John Golightly, Eugene Guillian, Phil Harvey, Mark Kos, Christine Kraus, Carsten Krauss, Cecilia Levy, Shirley Liu, Erin O’Sullivan, Helen O’Keefe¹, Sarah Quirk and all my friends at Queen’s University.

I would like to thank my beloved family: My beloved mother whose wisdom, patience, and support I could not have been without². My awesome father whom I inherited sense of humour and an inability to sing. My two brothers for having me as an older brother and for showing me respects, which I questionably deserve. All my aunts for raising me, and for all the delicious meals.

Thank you God, the time on Earth has been pleasant.

¹As spelt in “Energy Science: Principles, technologies, and impacts” by John Andrews and Nick Jelley

²Literally

Table of Contents

Abstract	i
Acknowledgement	ii
Table of Contents	iv
List of Tables	vi
List of Figures	viii
Chapter 1 Introduction	1
1.1 Evidence for Dark Matter	2
1.1.1 Dark Matter in Galactic Scale	2
1.1.2 Dark Matter in Clusters of Galaxies	4
Velocity Dispersion	4
1.1.3 Dark Matter in Cosmological Scales	5
Cosmic Microwave Background and WMAP	5
1.2 Dark Matter Candidates	6
1.3 Dark Matter Experiments	8
1.3.1 CDMS	9
1.3.2 XENON	10
1.3.3 PICASSO	14
Chapter 2 Dark Matter Detection with Liquid Argon	15
Chapter 3 DEAP-1 Detector	19
3.1 DEAP-1 Liquid Argon Chamber Design	19
3.2 Argon Purification System	20
3.3 Cryostat System	21
3.4 Water Shield	21
3.5 Pulse Shape Discrimination	25
3.6 DEAP-3600	27

Chapter 4 Backgrounds in DEAP-1	29
4.1 Gamma Background from ^{39}Ar	29
4.2 Alpha Background from ^{222}Rn	30
4.2.1 Radon Reduction Procedure	35
4.2.2 Radon Daughter Approximation	37
4.3 Background from Construction Materials	39
4.4 Cosmogenic Background	42
4.5 Measured Background Rate at SNOLAB	42
Chapter 5 Calibration with ^{22}Na coincidence gammas	46
5.1 Experimental Setup	47
5.1.1 Solid Angle Calculation for Source Position	52
5.2 DEAP-1 Monte Carlo	53
5.3 Slow Electronics	55
5.4 Fast Electronics	59
5.4.1 The Muon Veto Setup	62
5.5 DEAP-1 SCA Cut	65
5.6 Underground Electronics	65
Chapter 6 Result and Analysis	69
6.1 Understanding Pile-up Events	69
6.2 Cuts and Correction	74
6.2.1 Timing Cuts	74
6.2.2 PE Correction and Cuts	77
6.2.3 Stability of the high F_{prompt} Background	79
6.2.4 Z_{fit} Cut and PSD	82
6.3 Higher F_{prompt} Cut	84
6.3.1 Achievable PSD with Higher F_{prompt} Cut	88
Chapter 7 Conclusion	89
7.1 Detector Performance	89
7.2 Achievable PSD	90
Bibliography	92
Appendix A:	
List of runs use in the thesis.	97
A.1 Runs conducted at Queen's University	97
A.2 Runs conducted at SNOLAB	100

List of Tables

2.1	Scintillation parameters for electrons and nuclear recoil in noble liquids.	18
3.1	Minimum PSD requirement due to ^{39}Ar	27
4.1	The estimated alpha background per annum from the radon daughter deposition on the acrylic chamber.	39
4.2	Radioactive impurities of uranium, thorium and potassium	40
4.3	Expected neutron background from MC	40
5.1	Comparison between the expected rates from the Monte Carlo and the experimental data.	56
6.1	Pile-up prediction	70
6.2	Variables used for the pile-up calculation test.	74
6.3	Comparing the predicted neutron pile-up rate and the calibration data from run 1720–1725.	74
6.4	Achievable PSD with $F_{\text{prompt}} = 0.7\text{--}1.0$	83
6.5	Achievable PSD with F_{prompt} window of $0.85\text{--}1.0$	88
A.1	^{22}Na PSD data with 1 ns time bin and 50 mV/division	98
A.2	^{22}Na energy calibration	99
A.3	Neutron run	99
A.4	Standard trigger without a source for a muon study	99
A.5	Background runs on surface at Queen’s University	99
A.6	^{22}Na PSD data with 10 ns time bin and 50 mV/division. All runs before run 1488 use the slow output from the NaI PMT, which has wider timing resolution.	100
A.7	^{22}Na PSD data with 10 ns time bin and 20 mV/division	100
A.8	^{22}Na PSD data with 1 ns time bin and 50 mV/division	100
A.9	^{22}Na PSD data with 2 ns time bin and 50 mV/division	101
A.10	Runs used in the pile up study. 1711 is a run with SNO AmBe neutron source. 1720–1725 is a set of runs with both SNO AmBe neutron source and ^{22}Na γ s source.	101

A.11 ^{22}Na energy calibration with with 10 ns time bin and 50 mV/division	101
A.12 ^{22}Na a full spectrum DEAP-1 trigger	101
A.13 Background with 1 ns time bin and 50 mV/division setting	101
A.14 Background with 10 ns time bin and 50 mV/division setting	101

List of Figures

1.1	Rotation curve of NGC6503	3
1.2	The results from WMAP	7
1.3	Ionization yield vs. recoil energy in CDMS	11
1.4	Spin-independent WIMP-nucleon cross section upper limit	12
1.5	$\text{Log}_{10}(\text{S2/S1})$ in Xenon10	13
2.1	DEAP-3600 projected signals and backgrounds.	18
3.1	DEAP-1 assembly	20
3.2	DEAP-1 cryostat	22
3.3	DEAP-1 cryostat and chamber	23
3.4	Water shield	24
3.5	DEAP-1 pulses	25
3.6	Run 1295	27
3.7	ROI of run 1295	28
4.1	^{238}U decay chain	31
4.2	^{232}Th decay chain	32
4.3	Radon on surface 1	33
4.4	Radon on surface 2	34
4.5	Glove box and transfer port	36
4.6	DEAP-1 argon chamber's components	41
4.7	Total muon flux measured at various sites	43
4.8	Comparing backgrounds at Queen's Univeristy and SNOLAB.	45
5.1	Annulus photo.	48
5.2	Dimensions of the annulus detector.	49
5.3	Position and dimension of the annulus	50
5.4	Triple coincidence gamma calibration setup.	51
5.5	Angle θ used in solid angle calculation.	52
5.6	Optimum position from solid angle calculation	54
5.7	The ^{22}Na source is enclosed in a PET capsule.	55
5.8	Comparing the ^{22}Na from data and Monte Carlo.	56

5.9	Electronics diagram of the PMT bases.	57
5.10	NaI spectrum recorded with the CAMAC MCA.	58
5.11	The logic diagram for the triple coincidence gamma calibration with the fast electronics.	59
5.12	Annulus electronics diagram.	60
5.13	Timing of the coincidence trigger.	61
5.14	Comparing MC and data.	61
5.15	The triple coincidence gamma calibration geometry at Queen's Uni- versity.	62
5.16	Background run with annulus.	64
5.17	Run 393–395	64
5.18	The double coincidence gamma calibration geometry at SNOLAB. . .	66
5.19	The underground NaI PMT tag electronics diagram.	68
6.1	AmBe decay	71
6.2	Run 1711	72
6.3	Run 1711 energy ROI	73
6.4	Run 1720–1725	75
6.5	A high F_{prompt} event in the ROI from run 1721.	76
6.6	The zero crossing time of PMT 1, with gaussian fit to the peak in red.	77
6.7	The 511 keV peak position from run 1523	79
6.8	PE correction for 50 ns PSD run.	80
6.9	PE correction for 20 ns PSD run.	81
6.10	Comparing the high F_{prompt} events in the ROI	81
6.11	The stability of high F_{prompt} rate	82
6.12	Comparing Z_{fit} background	84
6.13	Achievable PSD with $F_{prompt} = 0.70$ – 1.00	85
6.14	The neutron survival probability as a function of the lower F_{prompt} cut.	86
6.15	The background rate as a function of the lower F_{prompt} cut.	87
6.16	Combined PSD data	87
7.1	Achievable PSD for various F_{prompt}	91

Chapter 1

Introduction

The term “dark matter” has a long history, dating as far back as 1844 when two different “dark matter” problems were identified. In that year, observations revealed that the planet Uranus had deviated from its calculated position by two arc minutes [1]. In the following year, J. C. Adams calculated “the position of a hypothetical planet whose gravitational effect on Uranus might be responsible for its disturbed motions” [2]. Adams, however, failed to convince astronomers to check his prediction. The same prediction was made independently by Le Verrier in 1846. Le Verrier was successful at convincing J.G. Galle, a German astronomer at the Berlin Observatory; the discovery of a new planet, the no longer “dark” Neptune, came shortly afterward. The other dark matter problem in 1844 was a prediction made by Bessel that Sirius was being disturbed by a companion star, which led to the discover of Sirius B afterward.

Today dark matter does not have many similarities with unobserved planets or stars like Neptune or Sirius B. The term “dark matter” in modern day refers to the unobserved astroparticle object based on the indirect evidence from gravitational

effects. In the past decades, the field of cosmology has provided evidence that there exists matter that has yet to be identified and directly observed; the term “dark matter” refers to this unknown matter. With this knowledge both cosmologists and particle physicists had postulated many theories about this missing matter and how it could be detected. Today, the search for dark matter has become a fast growing field with many experiments designed to detect and characterize it.

1.1 Evidence for Dark Matter

There is evidence for dark matter on many scales of the universe. Galaxy formation, astronomical observations of galaxies, cluster of galaxies, and the cosmological observation from the Wilkinson Microwave Anisotropy Probe (WMAP) all suggest that there exist large amounts of an unknown type of matter that has yet to be detected.

1.1.1 Dark Matter in Galactic Scale

The first suggestion of dark matter in galactic halos was perhaps made in 1970 by Freeman [3]. It was pointed out that the rotation curves of NGC 300 and M33, obtained from the 21 cm neutral hydrogen line, did not agree with the predicted Keplerian decline beyond the optical radii. Freeman came to conclude that “there must be in these galaxies additional matter which is undetected ... Its mass must be at least as large as the mass of the detected galaxy, and its distribution must be quite different from the exponential distribution which holds for the optical galaxy”. Figure 1.1 shows the rotation curve of NGC 6503. The observed rotation curve displays a characteristic flat behavior beyond the edge of the visible disks. The circular velocity,

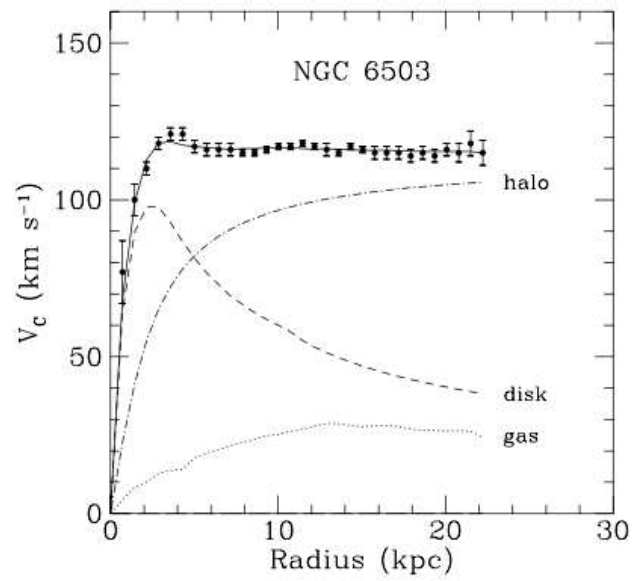


Figure 1.1: Rotation curve of NGC 6503. The contributions of gas, disk and darkmatter are represented by the dotted, dashed and dash-dotted lines, respectively. Figure was taken from [4].

$v(r)$ in Newtonian dynamics is given by equation 1.1

$$v(r) = \sqrt{\frac{GM(r)}{r}}, \quad (1.1)$$

where r is the distance from the center of the galaxy, G is a gravitational constant and, $M(r) \equiv 4\pi \int \rho(r)r^2 dr$, with the mass density profile $\rho(r)$. It can be seen that the mass density profile should be falling $\propto 1/\sqrt{r}$ beyond the optical disc. The flatness of the curve suggests the existence of a halo with $M(r) \propto r$ and $\rho \propto 1/r^2$ [4]. Vera Ruben and W. Ford [5] studied of the rotation velocity the Andromeda nabula by measuring the doppler shift of the H_α emission lines and they also suggested that the rotational velocity did not decrease with increasing distance from the galactic centre, i.e., the result disagrees with the Keplerian decline. The result shared similarity with the 21-cm study carried out by Freeman with the maximum velocity being slightly higher than in the 21-cm study.

In addition, the work by Ostriker and Peebles from 1973 [6] suggested that spiral galaxies require dark halos to stabilise them and prevent them from collapse into bar-like structures.

1.1.2 Dark Matter in Clusters of Galaxies

Velocity Dispersion

Extragalactic dark matter provided the first hint for the dark matter in the modern sense. It was discovered by Zwicky in 1933. He suggested that estimating the masses from the luminosities of the nebulae is inaccurate due to lack of information on the fraction of the nebula that luminous matter represents [7]. By applying the viral theorem to the Coma cluster [7], Zwicky estimated the mass of the cluster based on

the square of the average radial velocity. After the mass of the cluster is obtained, the average mass of nabulae was calculated to be 4.5×10^{10} the solar mass M_{\odot} [7]. The luminosity of an average nebula is about 8.5×10^7 the sun's luminosity, which makes the mass to light ratio of the nebulae about 400 times greater than that of the sun. This discovery suggested that there was a lot of non-luminous mass.

1.1.3 Dark Matter in Cosmological Scales

Cosmic Microwave Background and WMAP

According to the Big Bang theory, when the universe was young, it was smaller and much hotter and filled with hot hydrogen plasma. As the universe expanded and cooled, the photons from the hot plasma have been propagating ever since and grew fainter and less energetic. This radiation fills the entire universe and is called relic radiation or the cosmic microwave background (CMB). The CMB has a thermal black body spectrum peaking at a temperature of 2.725 kelvin, which corresponds to a frequency of 160.2 GHz. The CMB is approximately isotropic and fills the entire universe. The Wilkinson Microwave Anisotropy Probe (WMAP) is a mission to survey the CMB across the entire sky. It was started in July 2001. WMAP provided a map of the full cover of the microwave sky with a resolution of under a degree. The anisotropic pattern that exists in the map allows physicists and astronomers to construct a physical model of the universe. From the analysis of the CMB data obtained from WMAP, the angular power spectrum (see figure 1.2) was obtained. The angular power spectrum was fitted with the lambda cold dark matter (Λ CDM) model and the best fit model is a flat universe with a baryon fraction of $\Omega_b = 0.044 \pm 0.004$, a matter fraction of $\Omega_m = 0.27 \pm 0.04$, and a dark energy fraction of $\Omega_{\Lambda} =$

0.73 ± 0.04 [8]. So far, most of our known matter is in baryons, which means that 0.23 of the matter is still left undetected.

1.2 Dark Matter Candidates

Many possible candidates have been proposed to solve the dark matter problem: Baryonic dark matter, standard model (SM) neutrinos, sterile neutrinos, axions, supersymmetric (SUSY) particles, massive compact halo objects (MACHO), extra-dimensions, etc. [4]. Many of these candidates already have been ruled out, for example neutrinos due to their small mass and relativistic nature [4]. Galaxy formation requires the dark matter to be cold (non-relativistic) in order for matter to clump together. Also, the upper limit of neutrino masses are so small that it is not possible for them to contribute enough to the missing matter. Of all the candidates one of the most studied category of these candidates are Weakly Interacting Massive Particles (WIMPs). WIMPs only interact via gravity and the weak nuclear force, which means that they cannot be detected by standard electromagnetic radiation detectors.

One of the most promising techniques is direct detection. If our galaxy is surrounded by WIMPs, our planet should be passing through this WIMP cloud, making it possible to detect them via their interactions with matter. By measuring the spectrum of the energy transfer from the WIMPs in a nuclear recoil process, we can identify WIMPs. The recoil energy spectrum is roughly exponential e^{-aE} , where

$$a \propto \frac{\left(1 + \frac{M_T}{M}\right)^2}{v_0^2}, \quad (1.2)$$

with the target mass M_T , the WIMP mass M , the characteristic galactic velocity v_0

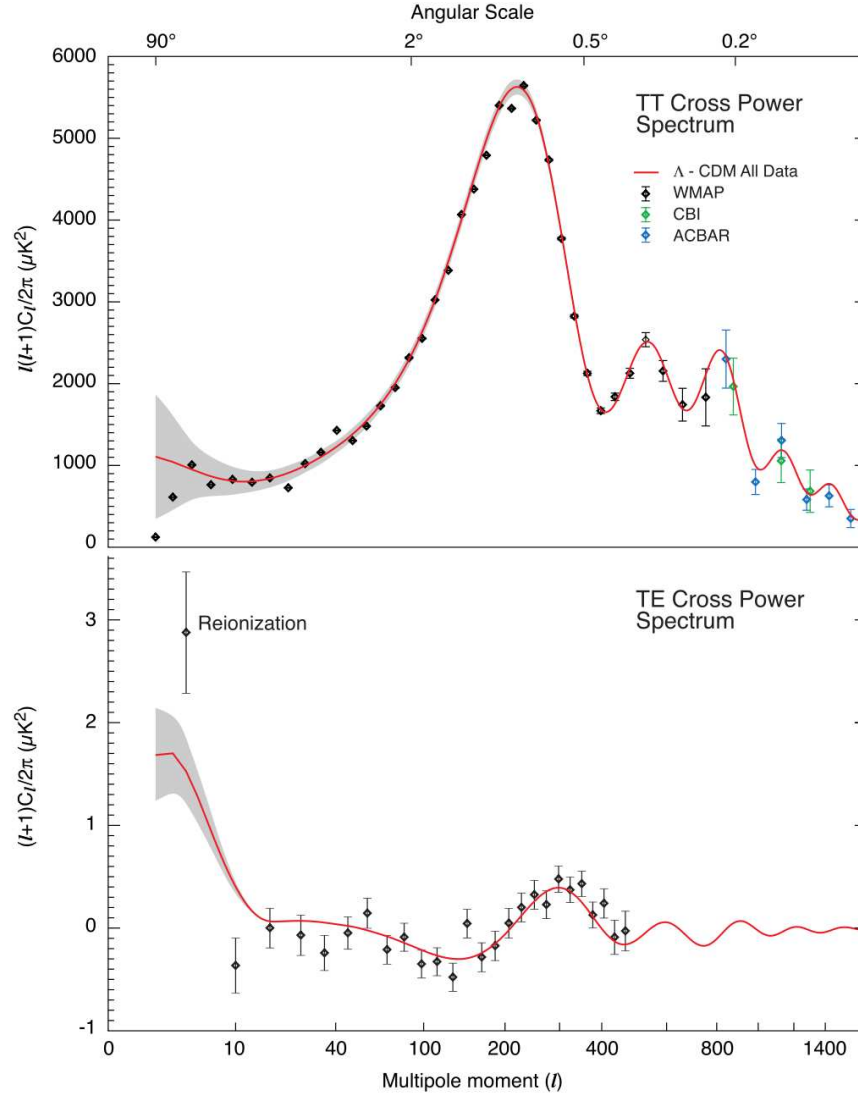


Figure 1.2: WMAP angular power spectrum. Top: WMAP temperature results (angular power spectrum), consistent with ACBAR and CBI measurements, as shown. The best-fit running index Λ CDM is shown. Bottom: TE (temperature polarization) cross-power spectrum. Figure was taken from [8].

and the constant a from the recoil energy spectrum [9]. The current experimental limits show that the rate is < 1 event/kg/year [10, 11] .

Neutrino experiments such as Super-Kamiokande, KamLAND and the Sudbury Neutrino Observatory have demonstrated that it is possible to detect weakly interacting astrophysical particles, provided that the background is low enough and the target volume is sufficiently large.

1.3 Dark Matter Experiments

The dark matter experiments can be categorized into two types: indirect and direct detection experiment. Direct dark matter experiments are aiming to identify the elastic scattering of WIMPs within the target volume, while the indirect experiments measure other particles that could be generated from the WIMPs annihilations such as neutrinos, positrons, anti-protons and gamma-rays [4]. The direct detection could be further categorized into spin independent and spin dependent interactions. In the spin independent scattering, the cross section is proportional to the square of the atomic mass number [12], while the spin dependent scattering cross sections are proportional to $J(J + 1)$ [4], where J is the total nucleon spin. In this section, we will introduce three direct detection dark matter experiments that use three of the most relevant detector technologies; solid state, liquid noble, and bubble detecting volumes. In the following chapter we will discuss direct dark matter detection using liquid argon, which is sensitive to the spin independent interaction.

1.3.1 CDMS

The Cryogenic Dark Matter Search (CDMS) [13, 11] uses germanium and silicon solid-state detectors. The detectors operate at ~ 40 mK inside the cold volume. CDMS uses both the charges and the phonons from ionizing radiation. The charges (electrons and holes) are drifted by a small electric field and collected on the electrodes, while the phonons are collected by super-conducting thin films. The fact that the ionization signal for nuclear recoils is suppressed relative to electron recoils is used to discriminate these events. Furthermore, the pulse shape of the phonon signal is used to discriminate against near surface events that could be otherwise misidentified as nuclear recoils due to the incomplete charge collection [13]. In CDMS, the ratio of ionization pulse height to phonon recoil energy (ionization yield) is used to discriminate nuclear from electron recoils with a rejection factor of $> 10^4$ [11]; this allows CDMS to reduce the dominating electromagnetic background. The ionization yield, however, could not distinguish the neutron background from the WIMP on an event by event basis. CDMS-II is situated 2,341 feet underground at the Soudan Underground Laboratory to reduce the muon flux, which could generate muon-induced neutron events. An active muon veto is applied to tag the remaining muon. CDMS-II uses polyethylene, lead and ancient lead to shield itself from some of the remaining background.

There are several means that can be used to distinguish neutron background from WIMPs.

- While neutrons often scatter several times in the detector, a WIMP will not.
- The WIMP-nucleon scattering rate is expected to be 5–7 times greater in Ge than in Si, while the neutron scattering rate is similar for the equal volume

of Si and Ge for 10 keV threshold and a neutron spectrum as expected from radioactivity in the rock.

- The recoil spectrum of the neutron elastic scattering is scaled by a factor of 2 in Si compared to Ge, the recoil factor for WIMP elastic scattering depends strongly on the WIMP mass.

The latest CDMS published result [14] has shown that in their set of data with appropriate data cleaning cuts, there are no event inside the WIMP signal band (shown in figure 1.3). With this result, CDMS has published their new dark matter limit, which is shown in figure 1.4. The CDMS collaboration is attempting to apply this technology to a significantly larger detector mass in order to increase the sensitivity. The SuperCDMS is expected to be operated at SNOLAB with a sensitivity to the spin-independent WIMP scattering cross-section of $1 \times 10^{-45} \text{ cm}^2$ at the 25 kg stage [11].

1.3.2 XENON

Located at Gran Sasso National Laboratory, the XENON10 [10, 15] experiment is a dual phase (gas-liquid) xenon time projection chamber. The detector uses 13.5 kg of liquid xenon as the active target. XENON10 measures both the scintillation and the ionization produced by particle interactions in Xe. The primary scintillation light (S1) is collected by top and bottom Photomultiplier tube (PMT) arrays. The ionization electrons are drifted through a 0.73 kV cm^{-1} electric field across the active xenon target and $\sim 13 \text{ kV}^{-1}$ across the liquid-gas boundary. Once drifted across the boundary into the Xe gas, the ionization is quickly accelerated and creates a burst of secondary scintillation (S2) from the collision with Xe atoms. The ratio between the

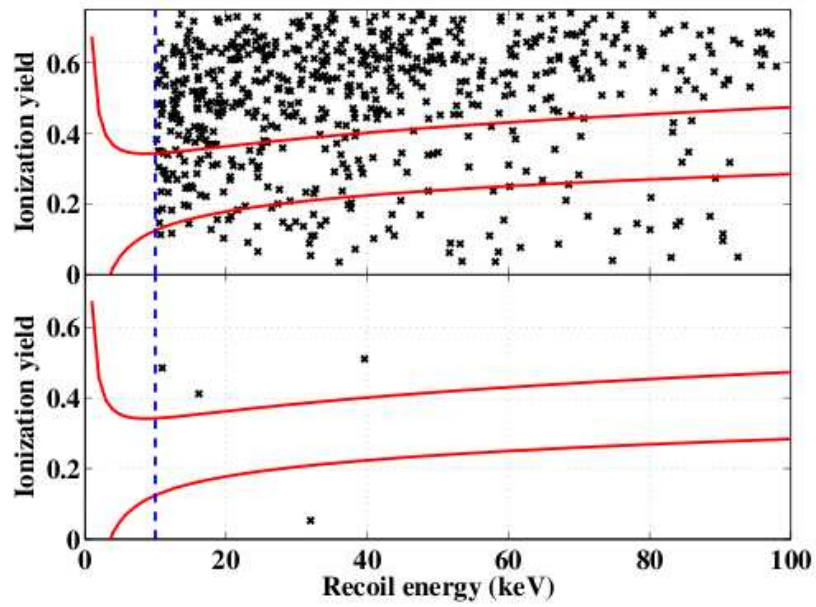


Figure 1.3: Top: Ionization yield versus recoil energy in all CDMS detectors included in this analysis for events passing all cuts except the ionization yield and surface electron recoil rejection cuts. The signal region is located between the two red lines. Bottom: Same as top but with surface electron recoil rejection cuts. From [14].

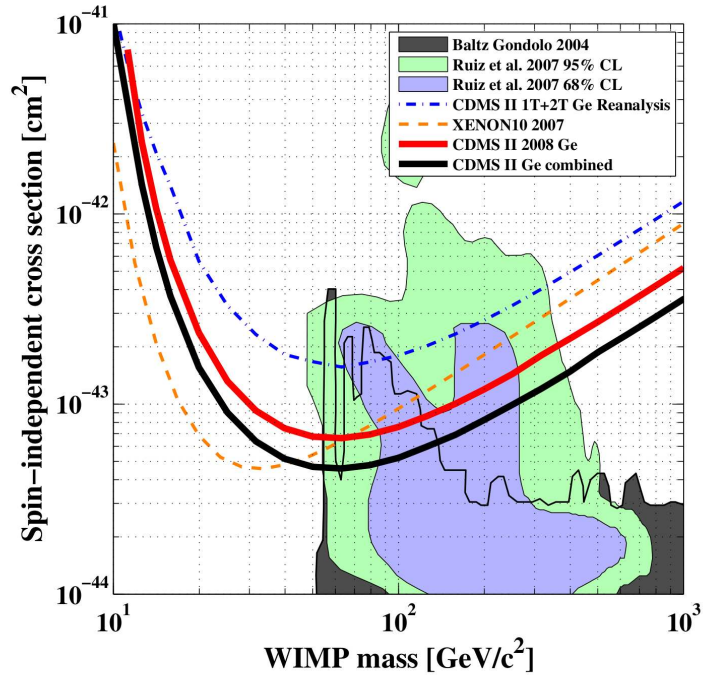


Figure 1.4: Spin-independent WIMP-nucleon cross section upper limits (90% C.L.) versus WIMP mass. The plot includes the results from both CDMS and XENON. The upper solid line represents limit derived from the new data set while the lower limit is the combined CDMS result. From [14].

two signals can be used to provide event-by-event discrimination between nuclear and electron recoil events. The difference between S2/S1 ratio for electron and nuclear recoil can be seen in figure 1.5. The dark matter limit set by XENON10 is shown in figure 1.4. The next generation detector, XENON100 uses approximately 100 kg target volume. Since the target volume is about ten times larger, it is expected to have a higher sensitivity by an order of magnitude from XENON10.

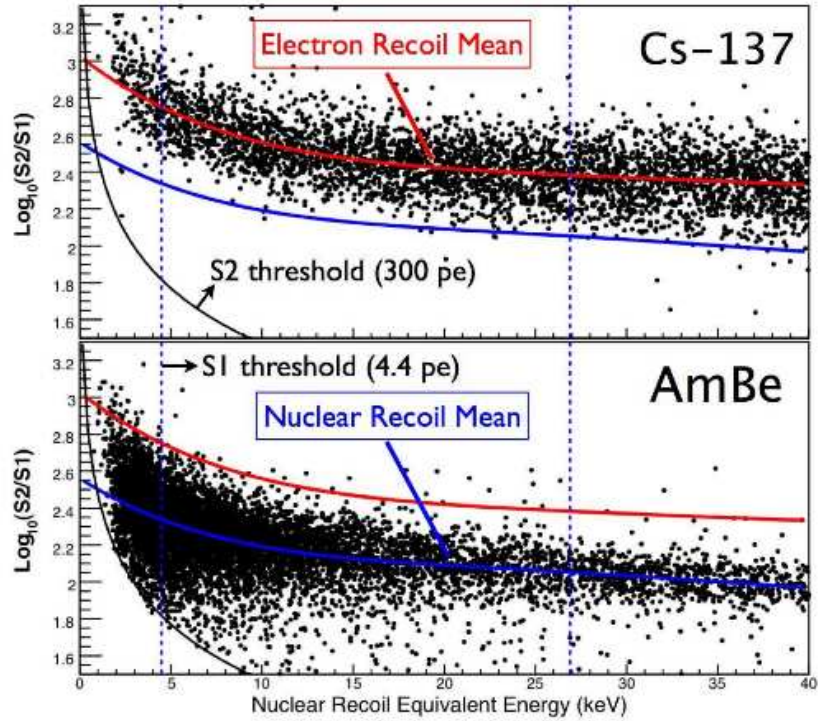


Figure 1.5: $\text{Log}_{10}(\text{S2/S1})$ as a function of energy from the ^{137}Cs and AmBe calibrations. The red lines are the mean $\text{Log}_{10}(\text{S2/S1})$ values of electron recoils, while the blue lines represent that of the nuclear recoils. The region between the two dash lines is the energy window used for the dark matter analysis. From [10].

1.3.3 PICASSO

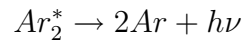
The PICASSO [12, 16] (Project In CANada to Search for Supersymmetric Objects) is a dark matter experiment, which uses superheated Freon (C_4F_{10}) droplets in a gel matrix as a detecting volume. It is currently located at the SNOLAB underground laboratory. The detector technology is based on the bubble chamber principle, where the detection mechanism relies on the meta stable superheated liquid to go through a phase transition, which is triggered by heat spike generated from a nucleus in the active mass that has obtained energy from the recoil from the incoming particle. When the phase transition occurs, it will produce pressure waves that can be detected with piezo-electric sensors. PICASSO detectors are threshold detectors, where a certain minimum amount of energy is required in order for the phase transition to occur. The threshold depends strongly on the operating temperature and pressure. This factor allows PICASSO to vary its threshold energy. Since each particle has a different energy deposition spectrum, the accurate threshold control will provide the differentiation between different particles.

One of the main advantages of PICASSO over the two previously mentioned experiments is its sensitivity to spin-dependent interactions due to Fluorine enhanced spin-dependent cross section.

Chapter 2

Dark Matter Detection with Liquid Argon

In the DEAP experiment, the possibility of using argon as a WIMP detector will be explored. Noble elements are known to produce scintillation light. In the DEAP detector, the scintillation process occurs when liquid argon transfers some of the incoming particle's energy into photons. Liquid argon scintillates in the vacuum ultraviolet (VUV) at 129 nm wavelength, with the width of approximately 10 nm [17]. There are two mechanisms in which the VUV from argon is produced; via excitons Ar^* or Ar^+ ions that recombine with the electrons. Equation 2.1 and 2.2 show the scintillation mechanisms via excitation and ion recombination respectively:



$$Ar^+ + Ar \rightarrow Ar_2^+, \quad (2.2)$$

$$Ar_2^+ + e^- \rightarrow Ar^{**} + Ar,$$

$$Ar^{**} \rightarrow Ar^* + \text{heat},$$

$$Ar^* + Ar + Ar \rightarrow Ar_2^* + Ar,$$

$$Ar_2^* \rightarrow 2Ar + h\nu$$

where h is the Planck's constant, ν is the frequency of the photon and *heat* corresponds to a non-radiative transition [17]. The excitation process dominates the luminescence process in the gaseous argon at normal temperature and pressure, however, the recombination luminescence becomes significant in liquid [18]. Kubota et al. [19] provide the evidence for the existence of the recombination luminescence; by applying an electric field of 10.0 kV/cm the light yield in argon was decreased by $(67 \pm 2) \%$. It was suggested that the decrease in light yield was caused by ions escaping the recombination process. The scintillation process has a good potential for detecting WIMPs. The incoming particle transfers energy to Ar to form excited dimers (eximers), which has two eigenstates, the singlet and the triplet state. The two eigenstates have very different lifetimes; $\tau_1 = 7.0 \pm 1.0$ ns and $\tau_3 = 1.6 \pm 0.1$ μ s for singlet dimer and triplet dimer respectively [20]. The amplitude of the singlet state, I_1 and the triplet state, I_3 depend on the linear energy transfer between the incoming particle and the argon nuclei. Because of a large difference between τ_1 and τ_3 , their amplitudes can be collected separately with relative ease. Since the electron interacts with electrons in the argon shell and the neutron interacts with the argon nuclei, the ratio between I_1/I_3 generated by those two are different and can be used

to distinguish them from one another.

Other advantages of using argon are as follow:

- Argon is present in the Earth's atmosphere at 0.93%, thus making it relatively inexpensive.
- Argon has high scintillation light yield.
- Argon has been widely used and its properties are well studied.
- Since argon's boiling point is just above that of liquid nitrogen, it will be relatively easy to make and maintain liquid argon. One can use an existing commercial cryogenic system that has been designed for liquid nitrogen.

A single-phase argon detector, such as DEAP, is simple and can have a large target mass. To compare to the experiments discussed in chapter 1, the 7 kg DEAP-1 and the DEAP-3600 have projected sensitivity of 10^{-44} cm² and 10^{-46} cm² respectively.

Table 2.1 summarizes the advantages of argon mentioned above and compares them with other noble liquids. These advantages led the collaboration to conclude that liquid argon is the most suitable target material for dark matter detection. However, like Achilles' heel, liquid argon also has disadvantages, which will be discussed in later chapters.

To give the reader a general idea about the background and signal region of DEAP-1, the WIMP recoil spectrum for argon is plotted with γ and neutron background in figure 2.1. From this figure it can be seen that the appropriate energy window ranged from 20–40 keV.

Table 2.1: Scintillation parameters for electrons and nuclear recoil in noble liquids from [21] and references there in.

Parameter	Ne	Ar	Xe
Light Yield ($\times 10^4$ photons/MeV)	1.5	4.0	4.2
Singlet time constant τ_1 (ns)	2.2	6	2.2
Triplet time constant τ_3	$2.9 \mu\text{s}$	$1.59 \mu\text{s}$	21 ns
I_1/I_3 for electrons	—	0.3	0.3
I_1/I_3 for nuclear recoils	—	3	1.6
$\lambda(\text{peak})$ (nm)	77	128	174
Rayleigh scattering length (cm)	60	90	30

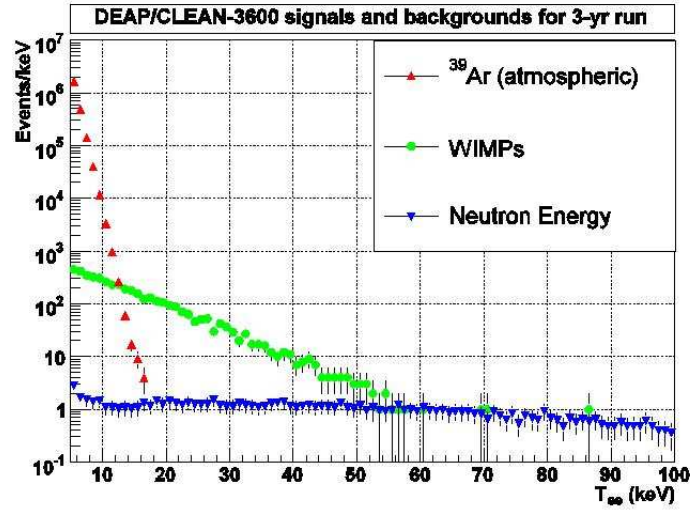


Figure 2.1: DEAP-3600 projected signals and backgrounds over the electron recoil energy range. From [22].

Chapter 3

DEAP-1 Detector

DEAP-1 is a prototype liquid argon detector. It was constructed and initially run at Queen's University. In October 2007, DEAP-1 completed its data taking above ground at Queen's university it was relocated to SNOLAB, which is located at 6800 foot level of Vale INCO's Creighton Mine in Lively, Ontario, where the muon-induced backgrounds is much lower. The muon reduction factor is discussed later in chapter 4.

3.1 DEAP-1 Liquid Argon Chamber Design

DEAP-1 uses approximately 7 kg of liquid argon as the WIMP target volume. As shown in figure 3.1, the liquid argon chamber is cylindrical with an acrylic light-guide and a photo multiplier tube (PMT) attached on each end of the cylinder to detect the scintillation light. The chamber is made from stainless steel with a 1/4" inner acrylic sleeve. DEAP-1 was designed to detect WIMPs via nuclear recoils in the liquid argon. The energy transfer from the incoming particle produces scintillation light via

the de-excitation of the liquid argon. The scintillation photons with a wave length of 128 nm will travel through thtetraphenyl-butadiene (TPB), a wavelength shifter coated onto the inner detector surface, and get shifted to the visible spectrum. The visible photons are collected by the 2 PMTs. Figure 3.1 shows the complete assembly of the argon chamber.

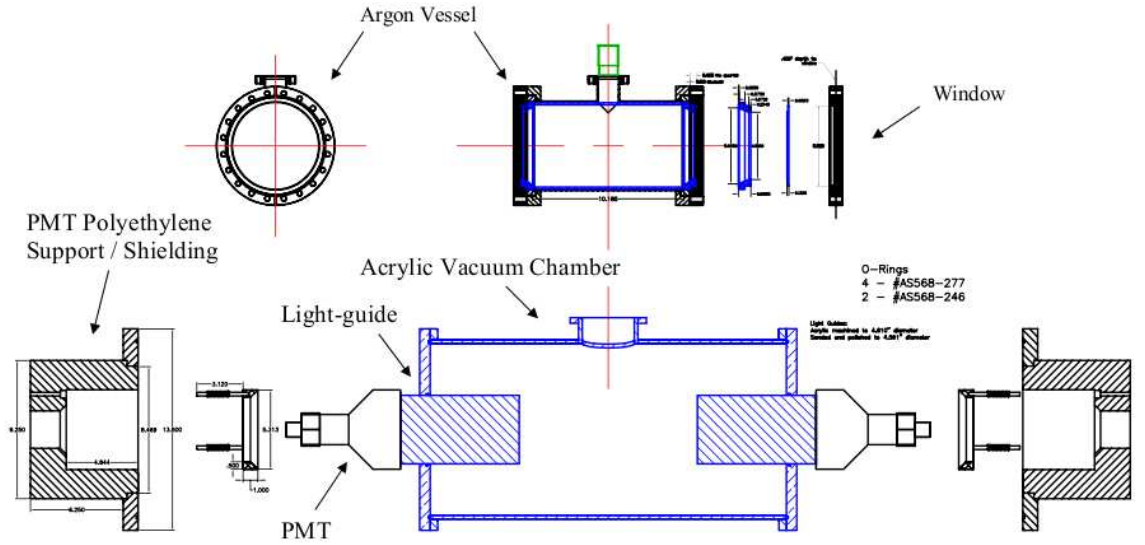


Figure 3.1: DEAP-1 argon chamber and insulating vacuum chamber from [23]. The inner acrylic chamber is coated with TPB on the inner surface and is placed inside the stainless steel chamber with two glass windows. The acrylic vacuum chamber is used to insulate the argon chamber. The scintillation light is collected by the two PMTs via the acrylic lightguides.

3.2 Argon Purification System

Argon from gas bottles is feed through a SAES Getter unit, which is designed to reduce impurities in the argon gas to <1 part per billion (ppb) [24]. These impurities can pose significant problems to the detector by absorbing the photons. In effect,

these impurities will quench the late scintillation lights [23].

3.3 Cryostat System

After the purification system the argon goes through a liquefier, which consists of a copper tube coiling inside the liquid nitrogen bath. The liquefier is shown in figure 3.2. The boiling point of liquid nitrogen is approximately 10 K lower than that of liquid argon. Therefore, the nitrogen must be kept under pressure to keep it above the freezing point of argon [23]. The cryostat was surrounded by the insulating vacuum to maintain the temperature. The vacuum chamber was made from acrylic with some stainless steel piping. Figures 3.3 shows the cryostats system and the argon chamber. Figures 3.1 shows the argon chamber's insulating vacuum with lightguides and PMTs. The inner argon detector and the vacuum system were designed to minimize radioactivities in argon

3.4 Water Shield

By moving the experiment underground, the muon-induced neutron background has been reduced substantially. However, there are still neutrons from the room, which are mostly created from the trace of ^{238}U and ^{232}Th . To reduce the neutron background, 400 water boxes were used with each water box containing 20 L (see figure 3.4).

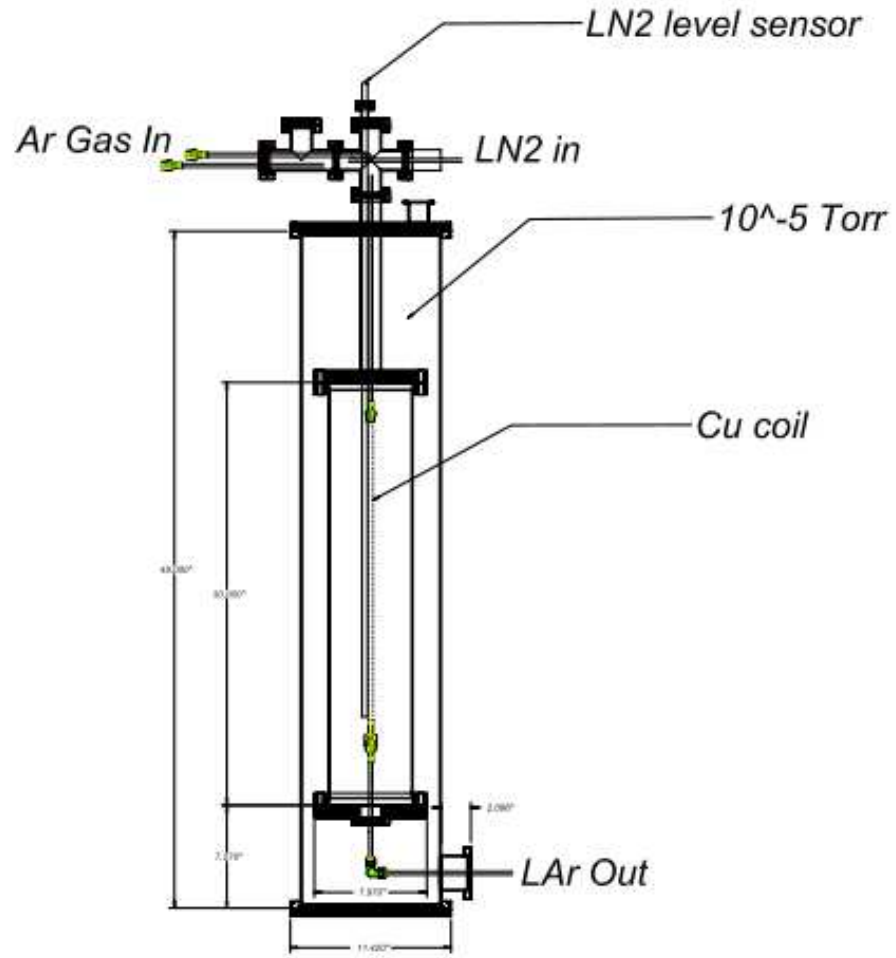


Figure 3.2: DEAP-1 cryostat and liquefier [23].

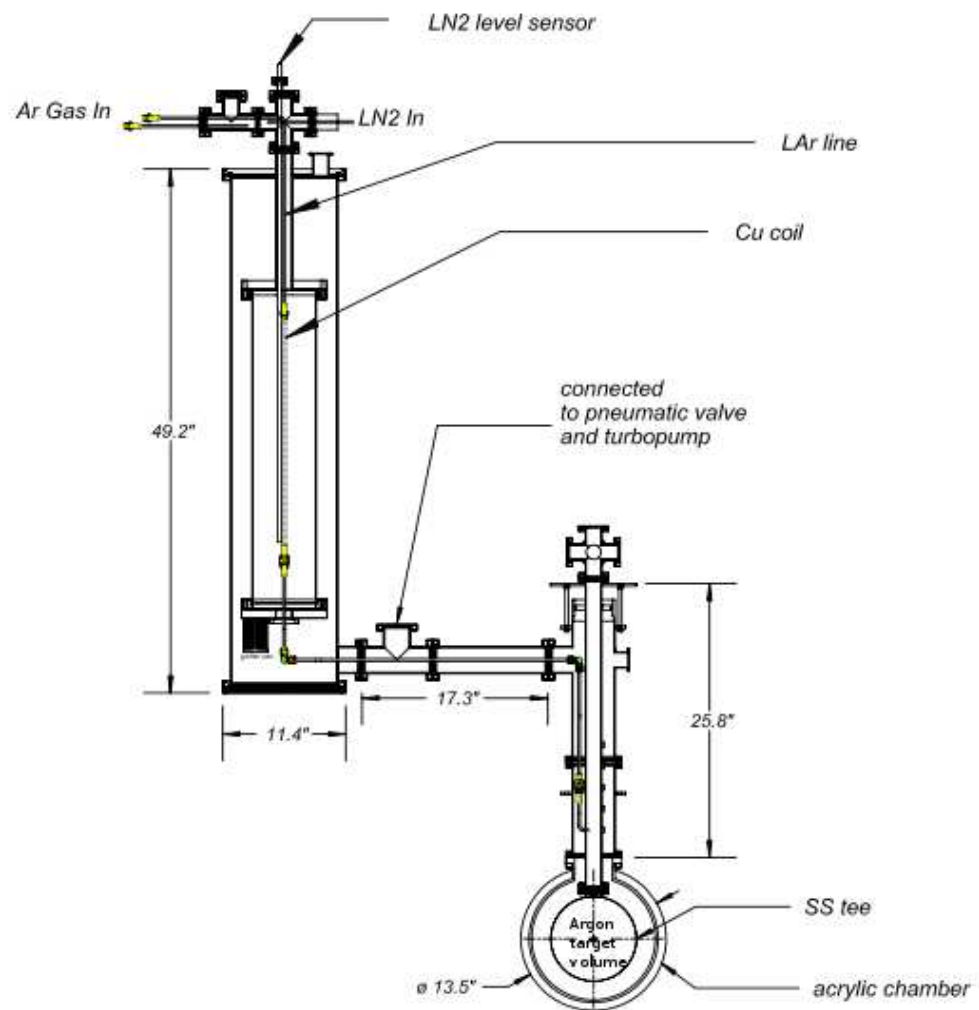


Figure 3.3: DEAP-1 cryostat and argon chamber [23].

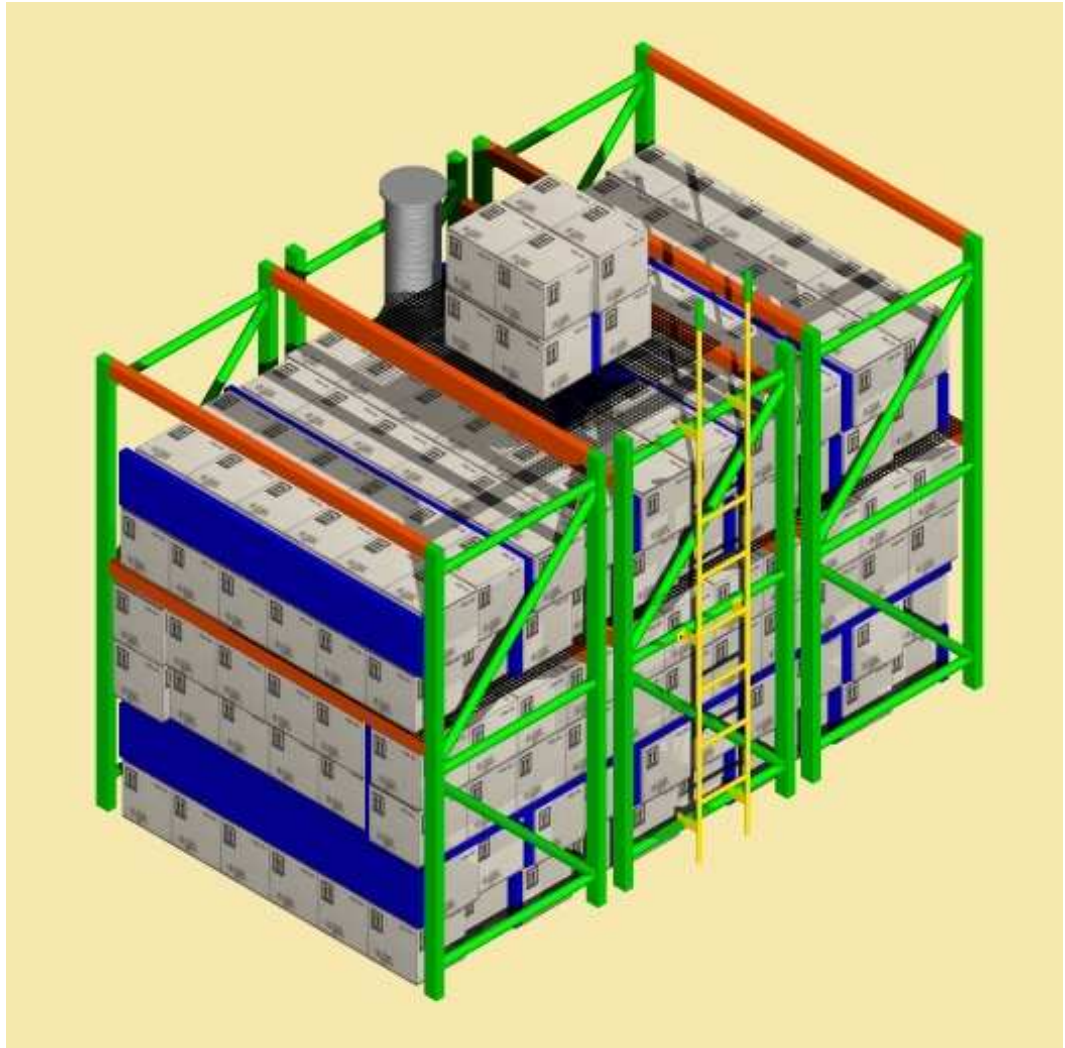


Figure 3.4: Diagram shows 400 water boxes, each box contains 20 L of water. The boxes are being used as a shield to reduce the neutrons background.

3.5 Pulse Shape Discrimination

In this section, we will discuss the pulse shape discrimination (PSD) power in DEAP-1. Further details can be found in the MSc thesis by Jeff Lidgard [23].

In order for DEAP experiment to be successful it is necessary to be able to distinguish the nuclear recoil events from the β^- background due to ^{39}Ar decays. DEAP uses the PMT pulse shape to discriminate the electromagnetic events, i.e. gamma and electrons, from the nuclear recoil events. This is possible due to the different decay times of light from the singlet and triplet dimers as previously mentioned in chapter 2. In DEAP-1, we use the ratio between the prompt light and the total light as a parameter to categorize a particle; this ratio is called $F_{\text{prompt}} = \frac{\text{PromptPE}}{\text{TotalPE}}$, where the prompt PE is the number of photo-electrons in the first 150 ns and the total PE is the number of photo-electrons from 0 to 9 μs . Figure 3.5 shows both the signal from a gamma-like event and a neutron-like event.

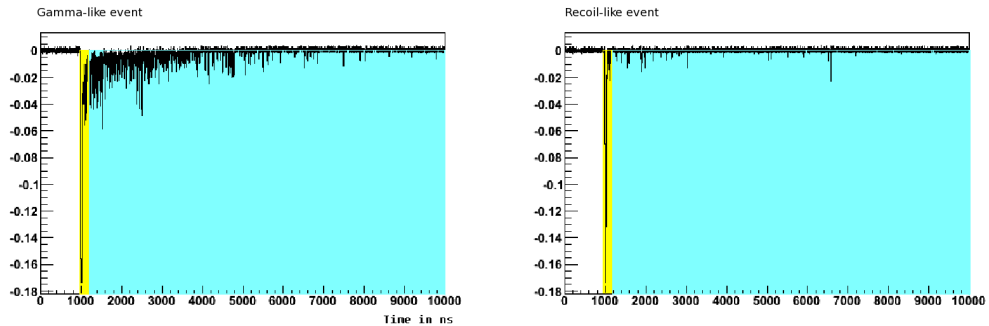


Figure 3.5: DEAP-1 events: The left image shows the gamma-like event. The right image shows the nuclear recoil like event. The yellow region represents the prompt window and the blue region represents the late light windows. [25]

The other constraint is the energy transfer. In the region of interest (ROI) of DEAP-1 we only consider events that generate 120 to 240 photo-electrons. Since the

photo-electrons yield per unit energy is about 2.8 PE/keV, the ROI corresponds to the energy range between 43 - 86 keV. Figure 3.6 shows a typical background run of DEAP-1. Figure 3.7 shows events that lie in the region of interest. The nuclear recoil window corresponds to the F_{prompt} window between 0.7 and 1.0. The dominating backgrounds in figure 3.6 are the β^- from ^{39}Ar ; it can be seen that at lower energy (low PE), the spectrum is very broad and the spectrum gets narrower as the energy increases. Therefore, it can be concluded that the discrimination power between β^- or γ and nuclear recoil events increases with the energy. The level of PSD required depend on the mass of the detector. Table 3.1 shows the PSD required for different detector sizes.

Table 3.1: Minimum PSD requirement due to ^{39}Ar [23].

Mass of Ar (kg)	Number of ROI events from ^{39}Ar per year	PSD required
7	3.9×10^6	2.6×10^{-7}
10	5.5×10^6	1.8×10^{-7}
100	5.5×10^7	1.8×10^{-8}
1000	5.5×10^8	1.8×10^{-9}

One of the main goals of the DEAP-1 detector is to demonstrate that the level of PSD required for DEAP-3600 can be achieved. The goal of this thesis is to achieve a high level of PSD with tagged calibration data.

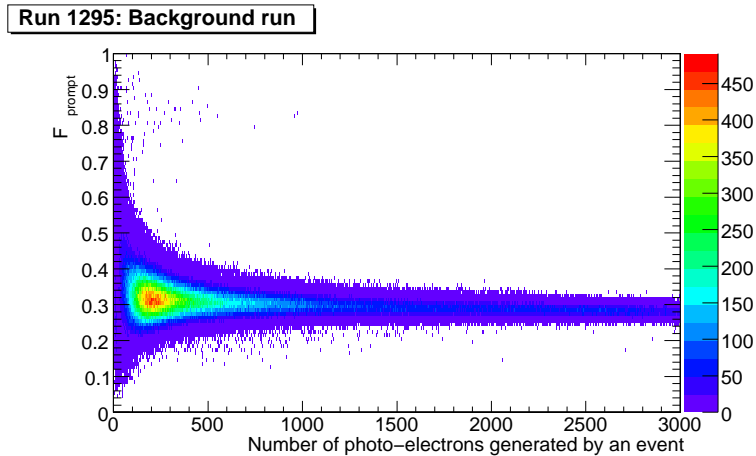


Figure 3.6: DEAP-1 run 1295: Standard background run with 1 ns time bin. The run was taken underground at SNOLAB with full waterbox shielding. The plot contains 2.85 million entries.

3.6 DEAP-3600

DEAP-3600 is the next generation of dark matter experiment, the construction will be starting in 2009. The DEAP-3600 detector will use 3600 kg of LAr as the target

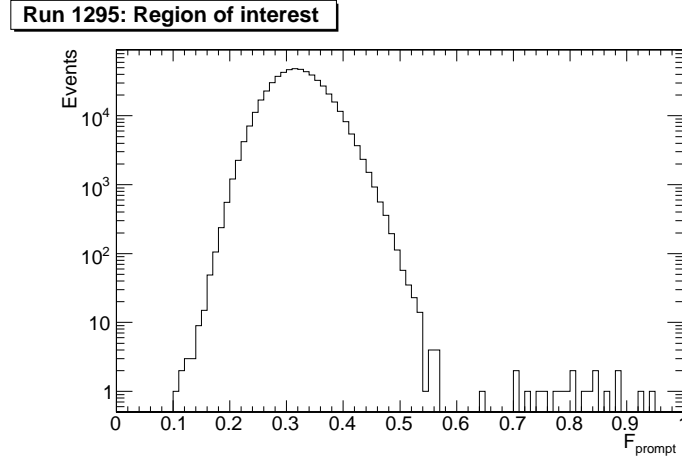


Figure 3.7: F_{prompt} distribution of events with 120 to 240 PEs. There are 19 events in the high F_{prompt} region (0.7–1.0). These events are nuclear recoil-like events.

volume. The argon will be housed inside a spherical acrylic chamber.

Chapter 4

Backgrounds in DEAP-1

There are several sources of backgrounds capable of producing scintillation events in DEAP-1 detector. Some of the backgrounds are associated with the location of the experiment: cosmogenic muons, neutron backgrounds from the room, etc. Many other backgrounds are associated with the detector: radioactivities in construction material, contamination in the bulk argon, and detector components. In a high sensitivity experiment such as DEAP-1, it is extremely important to understand and correctly estimate the backgrounds, since the sensitivity of the detector depends on it. In this chapter, we will discuss possible sources of background in DEAP-1.

4.1 Gamma Background from ^{39}Ar

The natural abundance of radioactive ^{39}Ar in the atmosphere, which is produced by cosmic rays, is the dominant background in DEAP. ^{39}Ar decay is shown in equation 4.1:



with β^- mean energy of 220 keV [26] and an end point of 565 keV [27]. Since standard commercial argon is extracted from air, it contains ^{39}Ar . Benetti et al[26] has measured the specific activity ^{39}Ar to be $0.87 \pm 0.02(\text{stat}) \pm 0.08(\text{syst})$ Bq per kg of natural argon. This number corresponds to 3.4×10^6 of events in the region of interest in DEAP-1 per year.

Since most of the ^{39}Ar in the atmosphere is cosmogenically produced, it is possible to find sources of argon, where ^{39}Ar has been reduced. However, since the half-life of ^{39}Ar is 269 years, it means that the argon reserve has to be isolated from the atmosphere for a considerable amount of time ($\sim 10^3$ years) before any significant depletion can occur. Several potential sources of depleted ^{39}Ar are the US National Helium Reserve (extracted from natural gas), underground wells, or water trapped beneath frozen lake, etc. The Depleted Argon group has shown that the ^{39}Ar contents in argon from the US National Helium Reserve is 20 times lower than in the atmosphere [28].

Currently, we are using commercial argon, which makes ^{39}Ar one of our main internal background. Since the ^{39}Ar is a β^- source, we should be able to use pulse shape discrimination to identify the ^{39}Ar background. In chapter 5, we will discuss the power to identify β and γ background with the pulse shape discrimination in more detail.

4.2 Alpha Background from ^{222}Rn

Two of the Earth's long-lived radioactive isotopes are ^{238}U and ^{232}Th with the half-lives of 4.468×10^9 and 1.405×10^{10} years, respectively. The products and half-life of these two decay chains are shown in figure 4.1 and figure 4.2. From those two figures

it can be seen that ^{222}Rn is one of the products of ^{238}U decay chain and ^{220}Rn is a product of ^{232}Th .

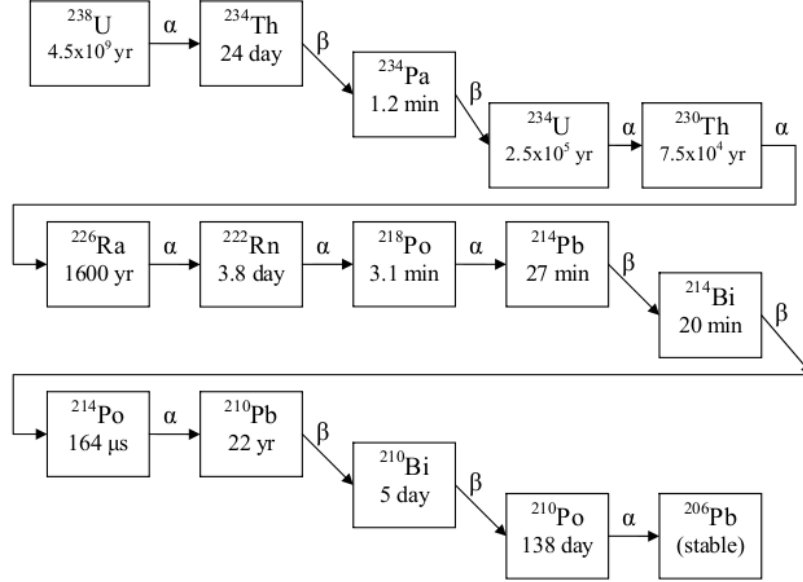
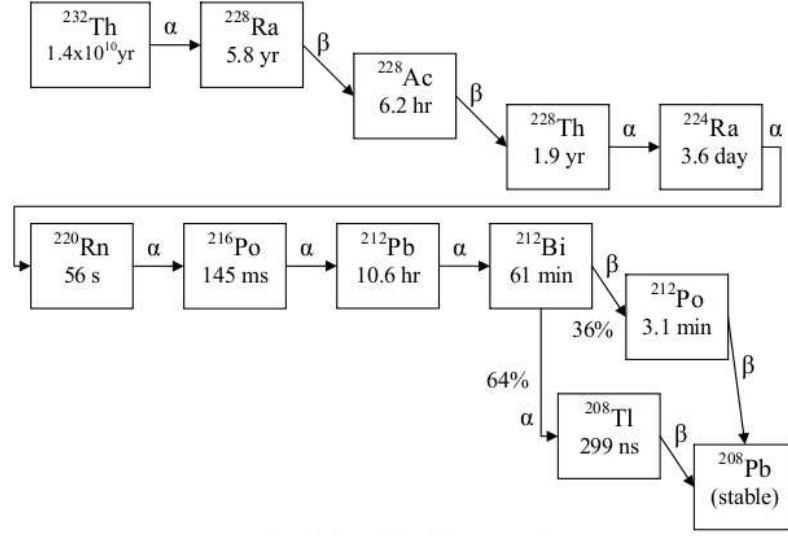


Figure 4.1: ^{238}U decay chain (Figure was taken from [23].)

The radon that is a major concern in DEAP-1 is ^{222}Rn from the ^{238}U decay chain due to the following reasons

- ^{222}Rn has a half-life of 3.8 days, which is long enough for it to travel and diffuse through materials.
- ^{222}Rn eventually decays to ^{210}Pb , which has a half-life of 22 years; this means that if the radon daughters deposit onto an inner detector surface, it will take a very long time for them to decay away. The typical decay rates for ^{222}Rn range from $\sim 10 \text{ Bq/m}^3$ of air in above-ground laboratories, to $> 100 \text{ Bq/m}^3$ of air underground at SNOLAB

Figure 4.2: ^{232}Th decay chain (Figure was taken from [23]).

The pulse shape discrimination in DEAP-1 should be able to separate most of the β backgrounds from the nuclear recoil events. However, one of the major concerns is that the radon daughters get embedded on the detector surface and only part of their energy gets deposited inside the detector. This embedding process might make the α event look like a nuclear recoil. One of the ways that the misidentification can occur is when the radon daughter gets deposited on the wavelength shifter; during the α decay, the final nuclear species could recoil into the argon and make it look like a nuclear recoil event (see figure 4.3). The other way is that if the radon daughter is embedded between the acrylic and the wavelength shifter. The α may lose some of its energy in the wavelength shifter. Since α 's have F_{prompt} similar to WIMPS, if they lose enough energy in the surface layer(s), then their final energy might be similar to the WIMP energy ROI (see figure 4.4).

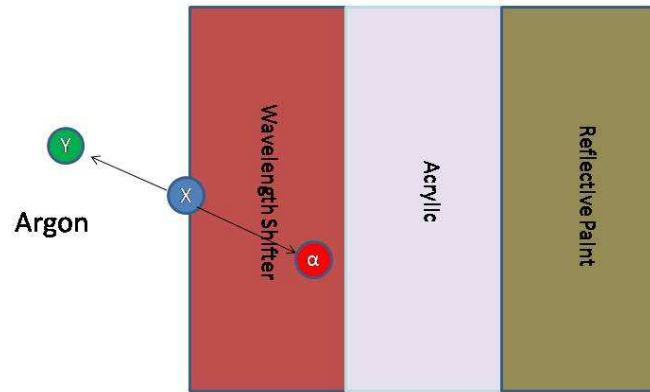


Figure 4.3: The radon daughter, X , gets deposited on the wavelength shifter. X decays into a new nucleus, Y and α . Y travels toward the argon volume and creates an event that look likes a nuclear recoil event.

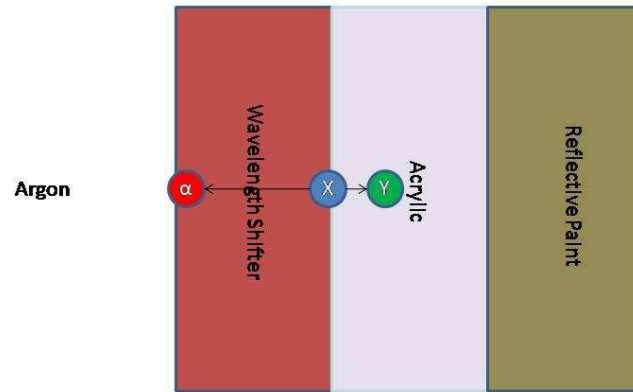


Figure 4.4: The radon daughter, X, gets deposited between wavelength shifter and the acrylic. As X decays, the α travels toward the argon and loses some of its energy in the wavelength shifter, which makes it more difficult for us to tag the α .

4.2.1 Radon Reduction Procedure

It was previously mentioned that the α from radon could be mistaken as a WIMP. Thus, it is one of the top priorities to reduce the radon background, since the capability to demonstrate the PSD power depends on the background reduction. One of the proposed solutions to reduce radon background is to minimize the detector exposure time to radon-contaminated gas and to sand off the chamber surface to reduce the surface contamination in the DEAP-1 detector. The chamber was sanded and painted with reflective TiO_2 paint inside a glove box, which is constantly being purged by nitrogen gas at 2 liters per minute to reduce the Rn content. Figure 4.5 shows the top view of the glove box. The nitrogen gas was obtained from boiling liquid nitrogen. However, to coat the wavelength shifter onto the chamber, it was necessary to transfer the chamber and the windows to the evaporation chamber, which is not connected to the glove box. To minimize the exposure time, the TPB was coated on the wire and attached to the frame inside the glove box and was transfer as one single piece. Once we transferred the chamber into the evaporation chamber, which was constantly purged by nitrogen, we immediately started the vacuum pump. After the coating was completed, we moved the chamber into the glove box via the transfer port. The chamber was placed in the transfer port for 24 hours. After the chamber was placed inside the glove box, we assembled the inner acrylic chamber and the windows of the DEAP-1 detector inside the stainless steel chamber, which was sealed with copper gaskets. The DEAP-1 detector then traveled to SNOLAB and was exposed to mine air during the installation for only a short amount of time (~ 6 minutes).

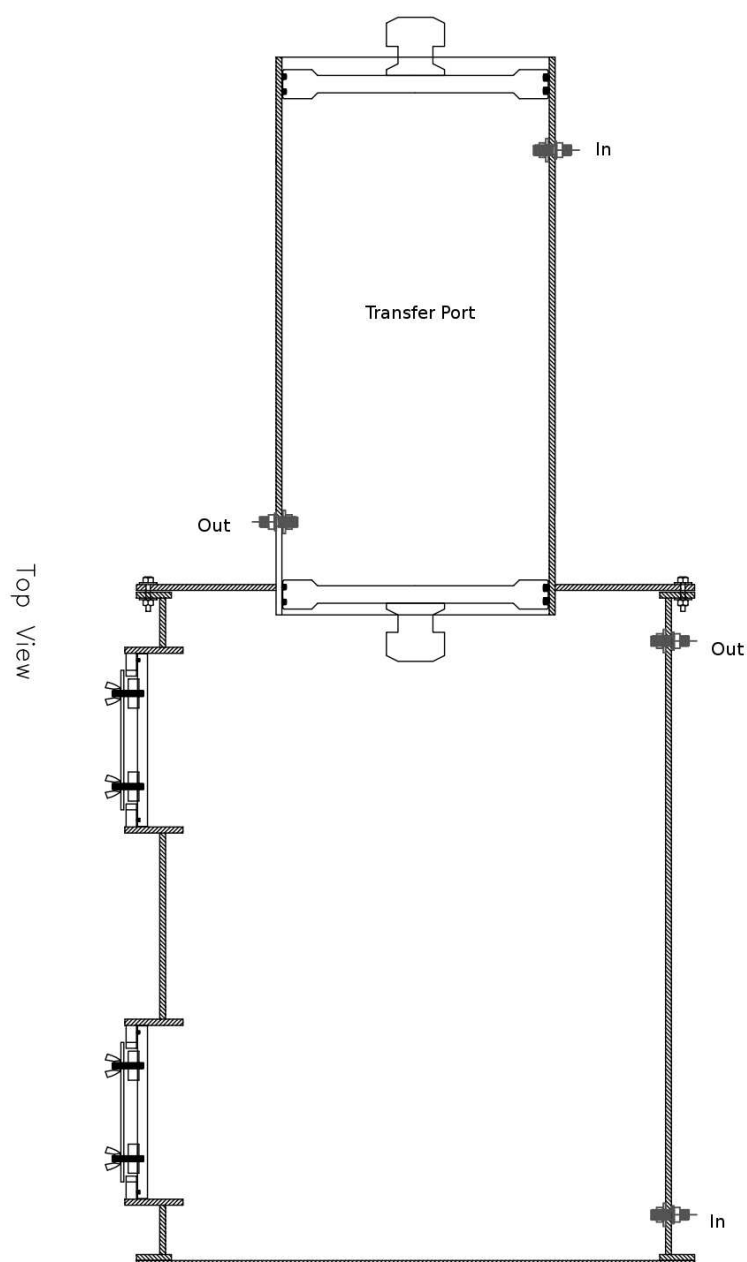


Figure 4.5: This diagram shows the top view of the glove box with the transfer port. The glove box was used to prepare the DEAP-1 chamber in a reduced-radon environment. The glove box and the transfer port each has a gas inlet and outlet. They are constructed from acrylic with reinforced metal bars and they are constantly being purged by the boil off gas from liquid nitrogen. Figure was drawn by David Bearse.

4.2.2 Radon Daughter Approximation

During the transfer process, the chamber gets exposed to open room air and the transfer chamber is filled with room air. To calculate how many radon atoms get deposited on the DEAP-1 chamber during the process we assume that all radon in the DEAP-1 volume (5.1 L) has a potential to decay and deposits its daughter on the surface of the detector. Thus, the amount of radon, N_0 , is equal to the radon concentration in the room multiplied by the volume of DEAP-1 chamber. Equation 4.2 shows how to calculate the number of radon daughters that get deposited on the DEAP-1 chamber, $N_{daughter}$,

$$N_{daughter} = N_0 \cdot \frac{t}{\tau_{Rn}}, \quad (4.2)$$

where $\tau_{Rn} = 4.737 \times 10^5$ seconds is the lifetime of ^{228}Rn , and t is the time of exposure. Radon daughter deposition can also occur in the transfer port, which is purged with nitrogen at 2 litres per minute. We assume that the nitrogen and the air inside the transfer port are completely mixed. This assumption means that for the amount of time that it takes the nitrogen to fill the transfer port, the radon concentration will be reduced by half. The number of radon in a transfer chamber, $N_{transfer}$, at any given time t , can be calculated by equation 4.3.

$$N_{transfer} = N_0 \cdot e^{-\frac{t}{\tau_{transfer}}}, \quad (4.3)$$

where $\tau_{transfer}$ is the time require to fill the transfer port volume divided by $\ln(2)$. Since the decay constants $\tau_{transfer}$ is much less than the τ_{Rn} , we assume that the exponential decay associated with $\tau_{transfer}$ is the dominating effect. The amount of time that the chamber spent in the transfer chamber is 24 hours. The number of radon daughters that is available to deposit on the chamber, $N_{daughter-transfer}$, can be

calculated by

$$N_{daughter-transfer} = \frac{1}{\tau_{Rn}} \cdot \int_0^{24h} N_0 \cdot e^{-\frac{t}{\tau_{transfer}}} dt. \quad (4.4)$$

The other concern is the radon in the liquid nitrogen dewar since we use the boil off to purge the glove box. The calculation of the radon contribution from the liquid nitrogen is similar to equation 4.2 except that N_0 is replaced by the number of radon in the liquid nitrogen, N_{LN2} .

Radon daughter deposition during the transportation from Queen's University to SNOLAB can also be calculated. Since the chamber is sealed, the concentration of the radon in the chamber will not get replenished. The radon daughter deposition during the transport, $N_{transport}$, is given by

$$N_{transport} = N_{LN2} \cdot (1 - e^{-\frac{t}{\tau_{Rn}}}). \quad (4.5)$$

The N_{LN2} level is very low due to the fact that the bottle generally get stored for a long time since the liquefying process and the radon has decayed away.

The radon daughter deposition from exposure to mine air can be calculated using equation 4.2 and replacing N_0 by the radon concentration in the mine, N_{mine} . Summing all these up we can calculate the upper limit of radon daughter deposition. After calculating the number of radon daughters deposited on the chamber, we can estimate the alpha background arising from the deposition. The number of α 's per annum was estimated for the exposure at Queen's University, the exposure in the transfer chamber, and the exposure in the mine. We use the decay constant of ^{210}Pb to determine the alpha decay since it has the longest half-life in the chain. The alpha activity from radon in Stirling Hall at Queen's University was measured to be 10 Bq/m³. This rate was used to calculate the radon concentration. Similarly, the radon activity in the mine, which was measured to be 100 Bq/m³, was used to calculate the

radon concentration in the mine. With the known background and exposure time, the alpha backgrounds from radon daughter deposition were calculated and summarized in table 4.1. These rates are low enough to allow a sensitive PSD calibration.

Table 4.1: The estimated alpha background per annum from the radon daughter deposition on the acrylic chamber.

Sources of Radon	Exposure Time (min)	Alpha per annum
Exposure to room air	10	1.3
Transfer port	1440	2.5
Exposure to mine air	6	8.0
Total		12.8

4.3 Background from Construction Materials

In this section, the backgrounds from the construction materials will be discussed and estimated. In a dark matter experiment, the number of signal events is so small that we virtually have to eliminate most of the backgrounds and understand backgrounds that we could not.

The materials were carefully selected to minimize the background in the process of constructing DEAP-1. Acrylic has very low levels of radioactive impurities, and therefore it is used wherever possible, for example, as light guide, inner argon chamber, and as construction material in place of metal when strength requirement could be reached. Some parts of the detector require strength for structural support, and difference in pressure, and endurance against the large temperature gradient. Therefore, it is necessary to use metals. The radioactivities associated with metals come from the small trace of uranium and thorium, which exist in most metals, and

their decay chains. Stainless steel was selected as a primary construction metal because it has relatively low activity. The welding of steel components was done with non-thoriated welding rods to reduce radioactive contamination. Other metals were also used, where less critical, to reduce the construction cost. Table 4.2 shows the construction materials for each part of the detector and the radioactive impurities associated with them. Figure 4.6 shows DEAP-1 components.

Table 4.2: Radioactive impurities of uranium, thorium and potassium [23, 29].

Component	Material	Mass(kg)	U(ppm)	Th(ppb)	K(ppm)
Chamber	Stainless steel	40	0.511	1.90	0.2177
PMTs	Mixed	0.420	28	31	60
Dark box	Aluminum	46.6	1550	580	3
Shield stand	Mild steel	500	100	100	100

The radioactive decay chains of ^{238}U and ^{232}Th are problematic. It can be seen in figure 4.1 and 4.2 that a number of α 's are emitted along these decay chains. These α 's can induce (α, n) reaction to produced neutrons. Monte Carlo simulation was used to estimate the expected number of neutrons produced from these radioactive impurities. The results are shown in table 4.3. From table 4.3, it can be seen that

Table 4.3: Expected neutron events per annum from Monte Carlo simulation [29] of uranium and thorium impurities in the detector [23, 30].

Component	Material	n/year/kg/ppb from ^{238}U	n/year/kg/ppb from ^{232}Th	n/year
Chamber	Stainless steel	0.124	0.138	13
PMTs	Mixed	10.53	9.6	126
Dark box	Aluminum	5.053	2.549	4.3×10^5
Shield stand	Mild steel	0.124	0.138	4.9×10^5

both the dark box and the shield stand are significant sources of neutrons. Although they generate similar numbers of neutrons, the shield stand is less critical because

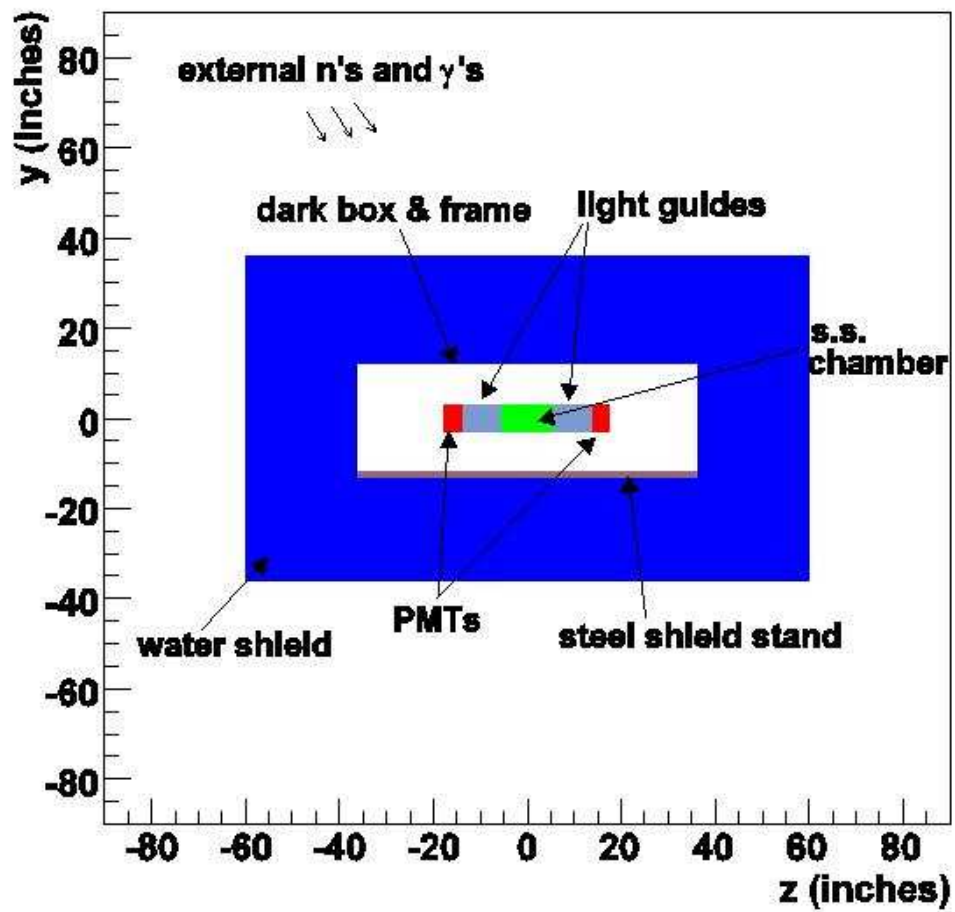


Figure 4.6: Diagram showing the DEAP-1 argon chamber's components. From [22]

of the water shielding between the stand and the detector. The dark box is a major concern as there is no shielding between the box and the detector. The material of the dark box will be replaced with a material that has lower a neutron background.

4.4 Cosmogenic Background

Cosmogenic muons caused significant background at Queen’s University. All naturally occurring muons on earth are created by cosmic rays. The protons from cosmic rays collide with atoms in the upper atmosphere and create pions. Pions decay into muons and neutrinos. These muons have very high energies and can create neutrons from spallation. The muons also can create Cherenkov radiation in the acrylic light guides. This effect is dealt with by doping acrylic with UV absorber, since Cherenkov light is mostly in the UV. In subsection 5.4.1, we further discuss how we deal with cosmogenic muon problem at Queen’s University. At SNOLAB, the muon flux is extremely low due to the 6800 ft of norite rock, which acts as a muon shield. Figure 4.7 shows the muon flux measured at various underground site. It can be seen that SNOLAB in Sudbury has extremely low background compare to other underground laboratories.

4.5 Measured Background Rate at SNOLAB

The high F_{prompt} background in the region of interest at SNOLAB were measured. Figure 4.8 compares the background rates at Queen’s Univerisy and at SNOLAB using the same set of cuts. It can be seen from the figure that the background rate at SNOLAB is a factor of 8 lower than at Queen’s University. This rate is much higher than the calculation pedicted. We are still working on understanding the background

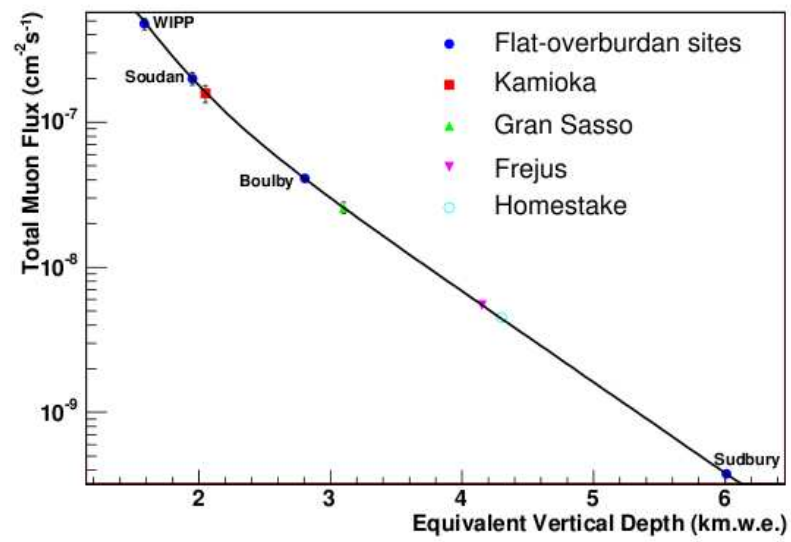


Figure 4.7: The total muon flux measured at various underground sites. [31]

and waiting for some materials to be assayed.

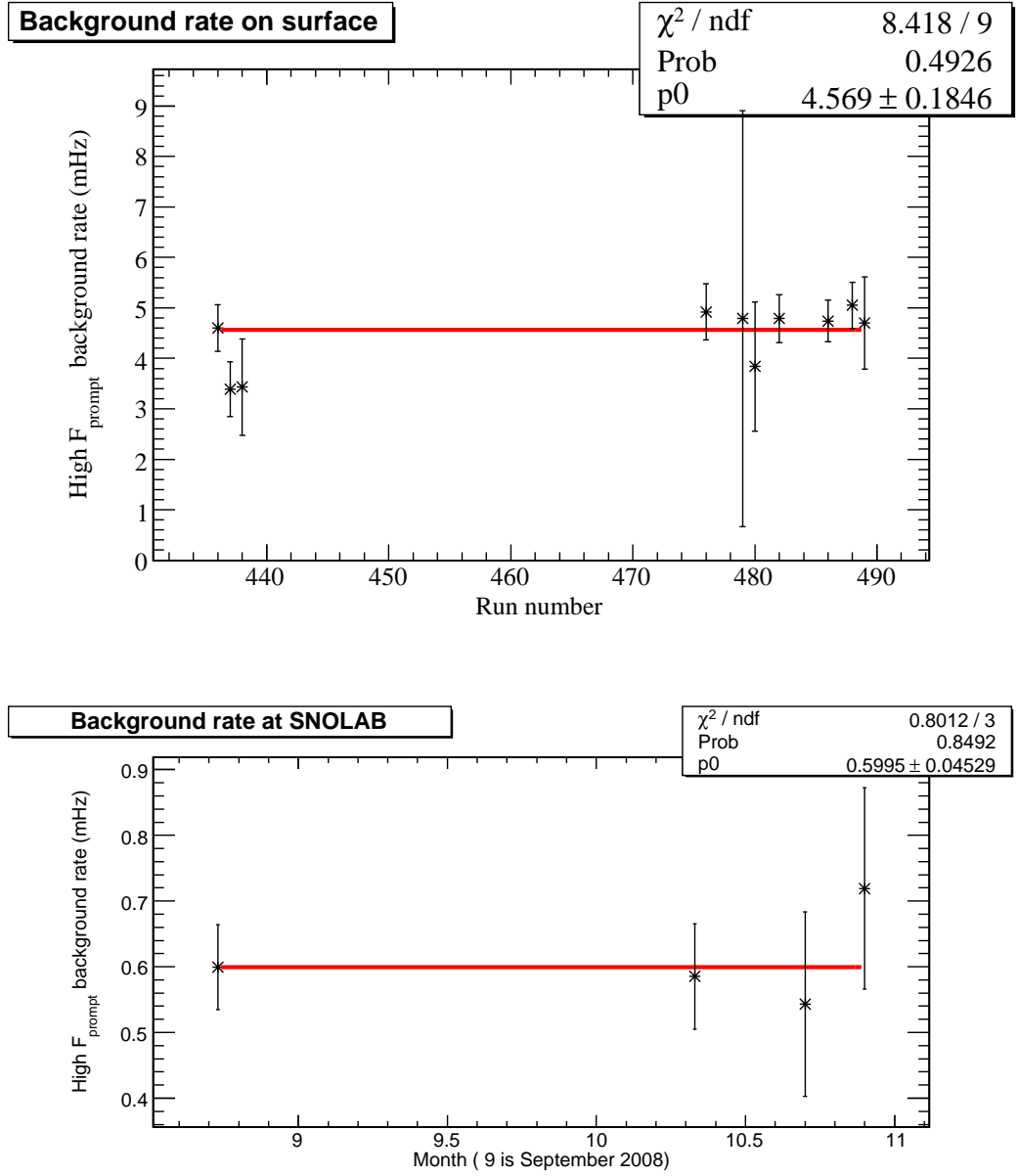


Figure 4.8: Top: The high F_{prompt} rates in the ROI from various background runs (see appendix A for more detail) at Queen’s University. The background rate in the WIMP window is 4.57 ± 0.18 mHz. Bottom: The high F_{prompt} rates in the ROI from various background runs (see appendix A for more detail) at SNOLAB. The background rate in the WIMP window is 0.60 ± 0.05 mHz.

Chapter 5

Calibration with ^{22}Na coincidence gammas

The largest internal backgrounds in DEAP-1 are from the natural abundance of ^{39}Ar , since ^{39}Ar decays to ^{39}K by emitting an electron with energy upto 0.565 MeV. DEAP-1 must be able to distinguish neutron events from these noises.

To demonstrate the discrimination power against the γ and β background, we required large number of these particles inside our detector. γ 's are preferred since they can be used from an external source. A γ source was implemented. DEAP-1 was running with only the double coincidence with double 511 keV back to back γ 's at first. However, the background was much higher than predicted. We concluded that the background was correlated and was caused by the muons. It was suggested that additional gamma from the source could be used as a tag. By using the additional γ , the triple coincidence gamma calibration was expected to be superior at reducing the neutron background in our coincidence window.

In addition, eight tons of water was used as a shield to further reduce neutrons

and other backgrounds. The water was put into 400 water boxes, each with 20 liter capacity. The space between DEAP-1 and the water boxes is filled in by the plastic wood, which has low radioactivity.

^{22}Na , which was encapsulated in aluminum, is used as the calibration source. The source strength was measured to be at 2.9 mCi in September 1984, which is about 175000 Bq in November, 2008. ^{22}Na decay gives a 546 keV positron and 1274 keV γ . Positrons scatter and come to thermal energies in aluminum before they annihilate with electrons to create γ rays:

$$e^+ + e^- \rightarrow 2\gamma. \quad (5.1)$$

Since the energy must be conserved, the two γ 's must have the combined energy of 1022 keV (2×511 keV). The angular momentum also must be conserved, the total momentum between two 511 keV/c γ rays must summed up to be roughly 3 keV/c, which can only happen if the γ rays are almost back-to-back, with angular separation that is slightly different from 180° . Berko and Erskine [32], and Hautojärvi [33] showed that in aluminum (both deformed and undeformed) the deviation from 180° has a half-width of 3 milliradians and thus is negligible in our case. These back to back 511 keV γ rays and the 1274 keV γ can be used as a triple coincidence calibration.

5.1 Experimental Setup

To detect the 1274 keV γ rays from the ^{22}Na decays, the annulus was used. The cylindrical annulus was made of four NaI crystals with one PMT attached to each section. Figure 5.1 shows photograph of the annulus and a PMT mounted with an NaI crystal at Queen's University. The NaI crystal convert the energy of particle and

turn it into visible photons, which get captured by the PMT. The dimensions of the annulus are shown in figure 5.2. A 3.25" NaI PMT was used to capture 511 keV γ rays. The diagram of the position of the annulus relative to the DEAP-1 detector is shown in figure 5.3. The distance between the annulus and the dark box is limited by the annulus's cart and DEAP-1's supporting frame. The experimental setup is shown in figure 5.4.

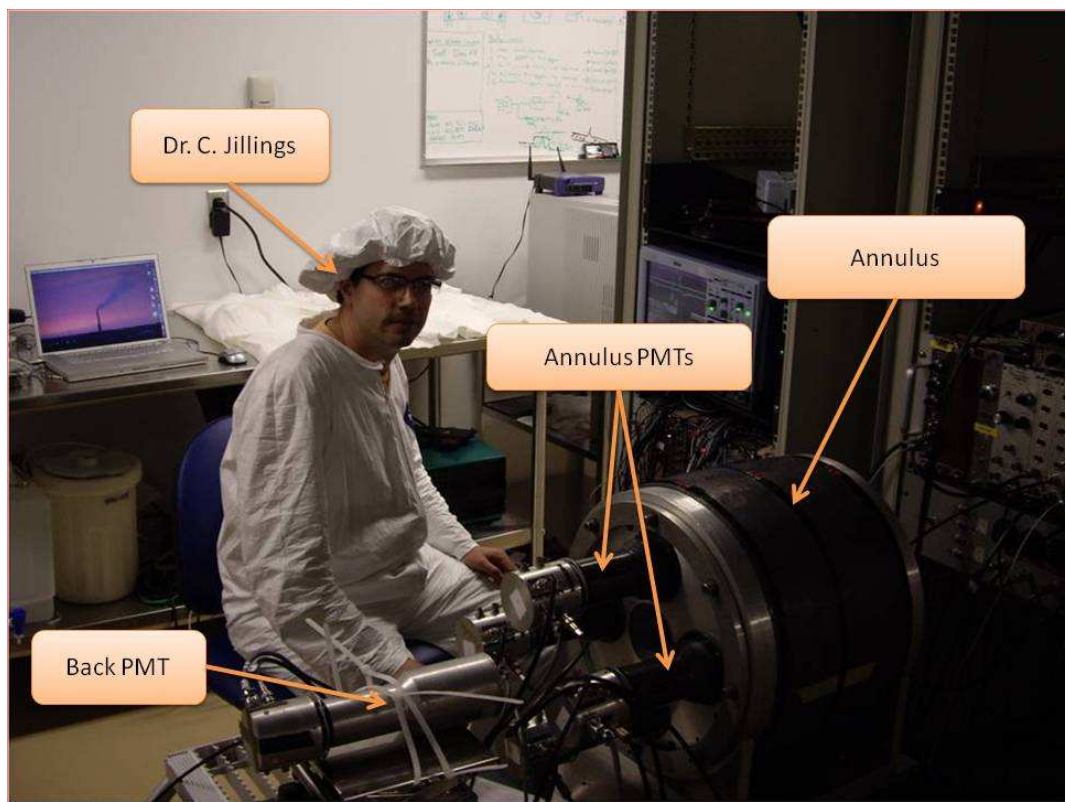


Figure 5.1: Photograph of an annulus and back PMT at Queen's University with DEAP-1 collaborator, Chris Jillings in the background.

Drawing not to scale.

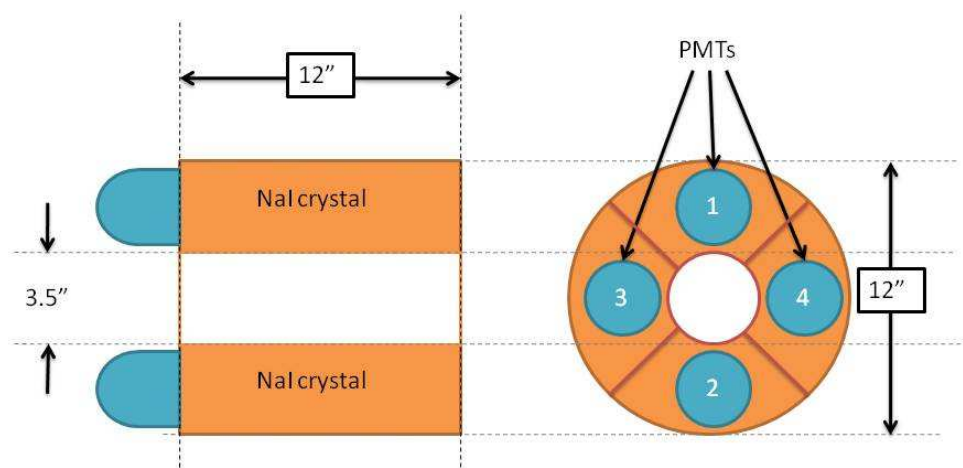


Figure 5.2: Dimensions of the annulus detector.

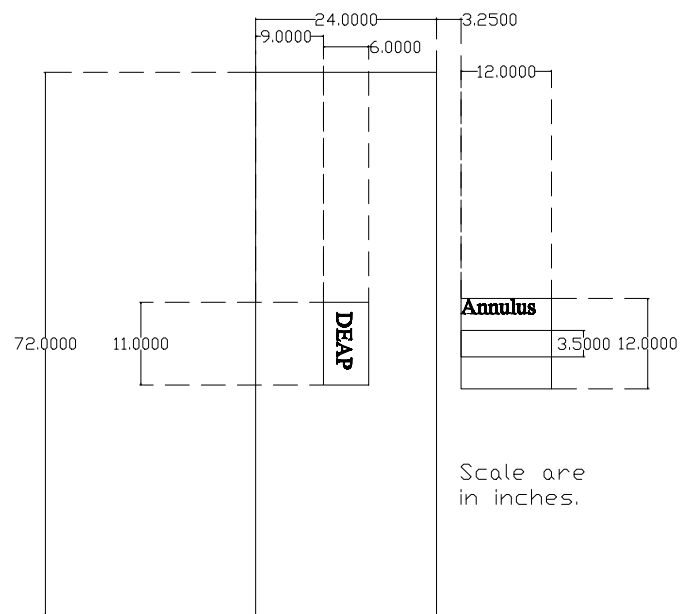


Figure 5.3: Geometry of DEAP-1 triple coincidence gamma calibration setup with dimension in inches. The annulus is placed 3.25" from the dark box, which is the closest possible position. The distance x refers to the position of the source from the opening of the annulus as shown in the diagram.

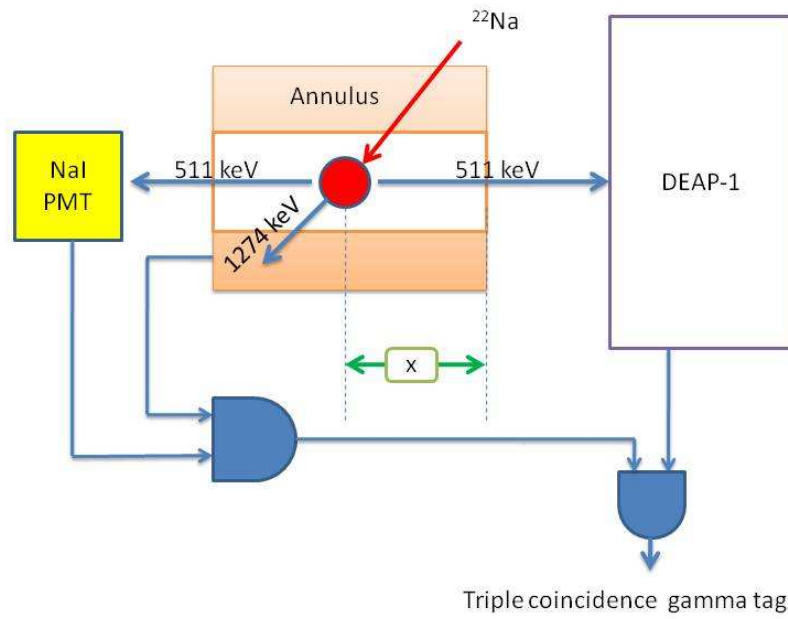


Figure 5.4: Triple coincidence gamma calibration setup with ^{22}Na source and the annulus. The figure summarizes how the global coincidence tag is generated. The 1274 keV signal from the annulus is in coincidence (level 2) with the 511 keV γ from the back NaI PMT creates a tag signal. Global trigger is generated if the tag signal is in coincidence with a DEAP-1 signal. The distance “x” refers to the position of the surface from the opening of the annulus.

5.1.1 Solid Angle Calculation for Source Position

From the geometry in figure 5.3, we determined the optimum position for the source. The calculation was done under the assumption that the rate is proportion to the product between the solid angle of the annulus and the solid angle of DEAP-1 detector; this assumption should be valid since the flux and the cross section are constants. The annulus was modeled as a cylinder and DEAP-1 was model as a rectangle. The solid angle of the annulus could be calculated by subtracting two open ends from 4π . The open ends of the annulus can be modeled as a disk. The solid angle of a disk is given by equation 5.2

$$\int_0^{2\pi} \int_0^\theta \sin \theta d\theta d\phi = 2\pi \int_0^\theta \sin \theta d\theta = 2\pi [-\cos \theta]_0^\theta = 2\pi(1 - \cos \theta) \quad (5.2)$$

where the angle θ is shown in figure 5.5. The solid angle of the open end on the

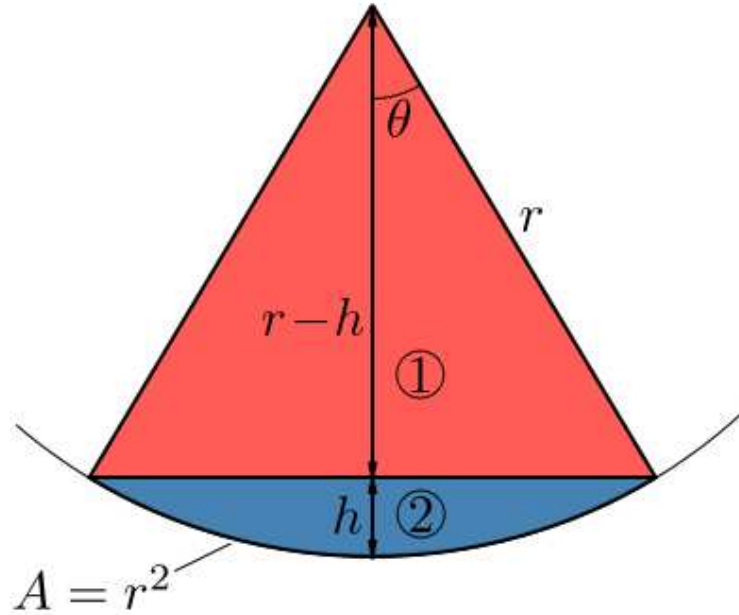


Figure 5.5: Angle θ used in solid angle calculation.

DEAP detector side can be written as

$$S_1 = 2\pi \cdot \left(1 - \frac{x}{\sqrt{x^2 + 1.75^2}} \right) \quad (5.3)$$

where “x” is the distance of the source location from the edge of the NaI crystal and 1.75” is the inner radius of the annulus. The solid angle of the open end on the other site can be written as

$$S_2 = 2\pi \cdot \left(1 - \frac{12 - x}{\sqrt{(12 - x)^2 + 1.75^2}} \right), \quad (5.4)$$

where 12” is the length of the annulus.

By subtracting solid angles of both ends from 4π , the solid angle of the annulus can be written in the following form

$$S_{Ann} = 2\pi \cdot \left(\frac{x}{\sqrt{x^2 + 1.75^2}} + \frac{12 - x}{\sqrt{(12 - x)^2 + 1.75^2}} \right) \quad (5.5)$$

The solid angle of DEAP-1 was approximate as a solid angle of a rectangle and can be written as;

$$S_{DEAP} = 4 \cdot \arctan \left(\frac{5.5}{x + 15.25} \right) \left(\frac{3}{\sqrt{(x + 15.25)^2 + 3^2}} \right), \quad (5.6)$$

where 5.5” is half of the length of DEAP-1 argon chamber, 15.25” is the distance from the annulus to the center of the chamber, and 3 is the radius of the chamber(all dimensions are in inches).

From equation 5.6 the optimum distance of the source from an opening of the annulus was calculated and plotted in figure 5.6.

5.2 DEAP-1 Monte Carlo

The standard DEAP-1 Monte Carlo written in GEANT4 and used by the collaboration, was used as a base model. GEANT is an acronym for “Geometry and tracking”.

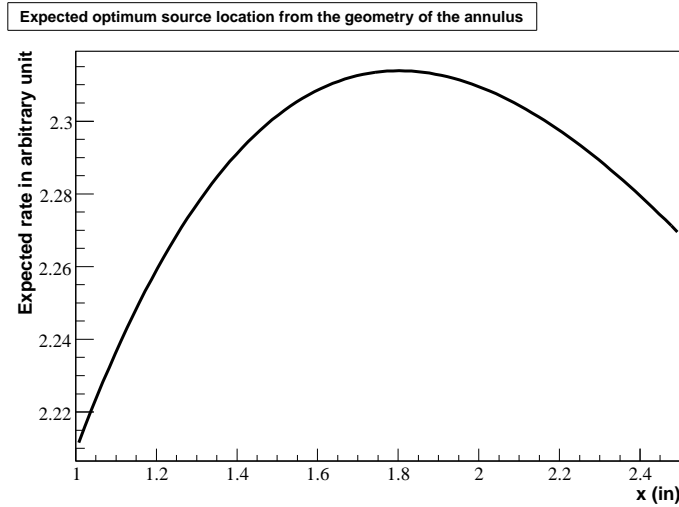


Figure 5.6: Optimum position from solid angle calculation

It is a software toolkit for the simulation of the passage of particles through matter [34]. The four NaI crystals from the annulus, the NaI crystal from the back PMT, and the lead shield were added to the DEAP-1 Monte Carlo. The two back-to-back 511 keV γ 's (90% probability), and the 1274 keV γ were used to simulate the ^{22}Na source. Monte Carlo simulations were generated at various source positions to determine the optimum source position inside the annulus. The comparison between the Monte Carlo and the data is shown in figure 5.14.

DEAP-1 Monte Carlo was also compared to the underground data. One of the largest uncertainties is the source position. Since it was moved underground, the source was enclosed in a polyethylene terephthalate (PET) capsule in an unknown geometry. Figure 5.7 shows the source with the PET capsule. The uncertainties from the Monte Carlo are largely dominated by the uncertainty in source position. Table 5.1 compares data with Monte Carlo. From the table it can be seen that there are discrepancies between DEAP-1 rate, and DEAP-1 rate in ROI of the data and

Monte Carlo. The comparison between the ^{22}Na spectra of data and Monte Carlo is shown in figure 5.8. The Monte Carlo spectrum was generated by convoluting the energy deposition in the argon with the DEAP-1 energy response function. The energy response function was calculated from the standard deviation (σ) of the 60 keV γ peak from the AmBe and the 511 keV γ peak from the ^{22}Na . There is a large discrepancy between the data and DEAP-1 Monte Carlo, we suspected that there is a bug in a Monte Carlo.

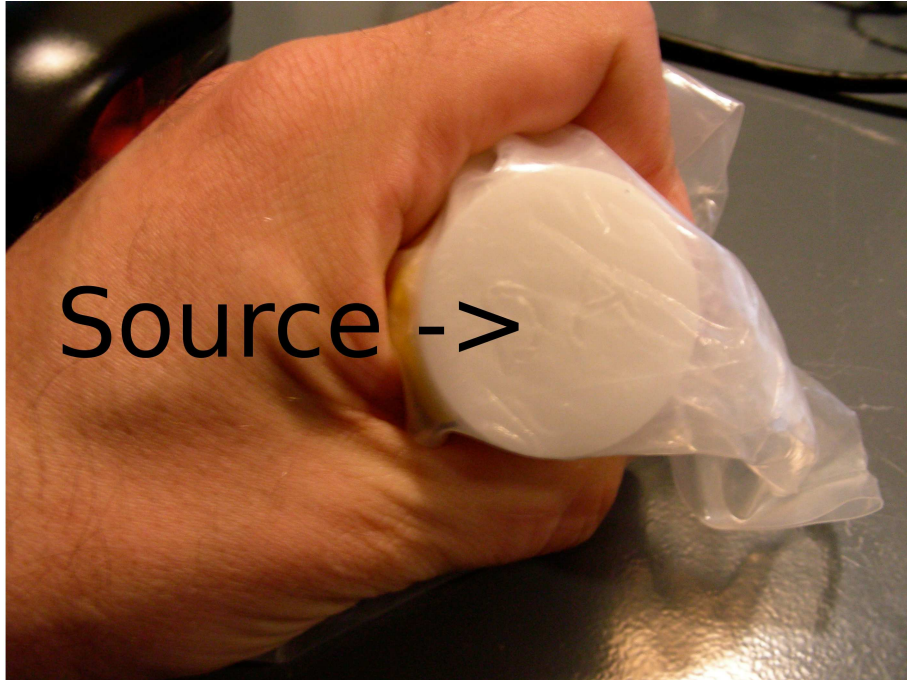


Figure 5.7: The ^{22}Na source is enclosed in a PET capsule.

5.3 Slow Electronics

In this section, we will discuss the first-attempt triple coincidence gamma tagging system and electronics setup. The annulus was used to tag the 1274 keV γ and the

Table 5.1: Comparison between the expected rates from the Monte Carlo and the experimental data.

	MC rate (Hz)	Data rate (Hz)
NaI rate	9700 ± 3500	8900 ± 100
DEAP-1 rate	7910 ± 960	9000 ± 100
DEAP-1 rate in ROI	600 ± 80	396 ± 6
Coincidence rate	1040 ± 240	1060 ± 10

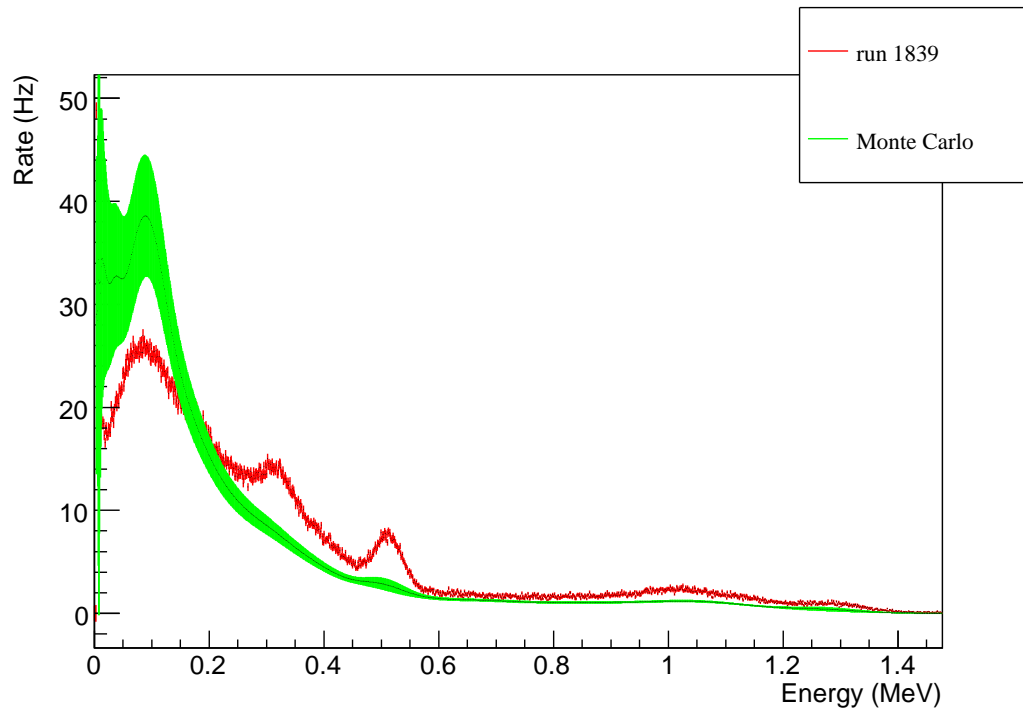


Figure 5.8: Comparing the ^{22}Na from data and Monte Carlo.

back NaI PMT was used to tag the 511 keV γ (see figure 5.4). The slow electronics refers to the use of the slow output from the annulus PMTs. The diagram of the PMT base is shown in figure 5.9, where the slow signal is taken from the dynode 8 through the preamplifier.

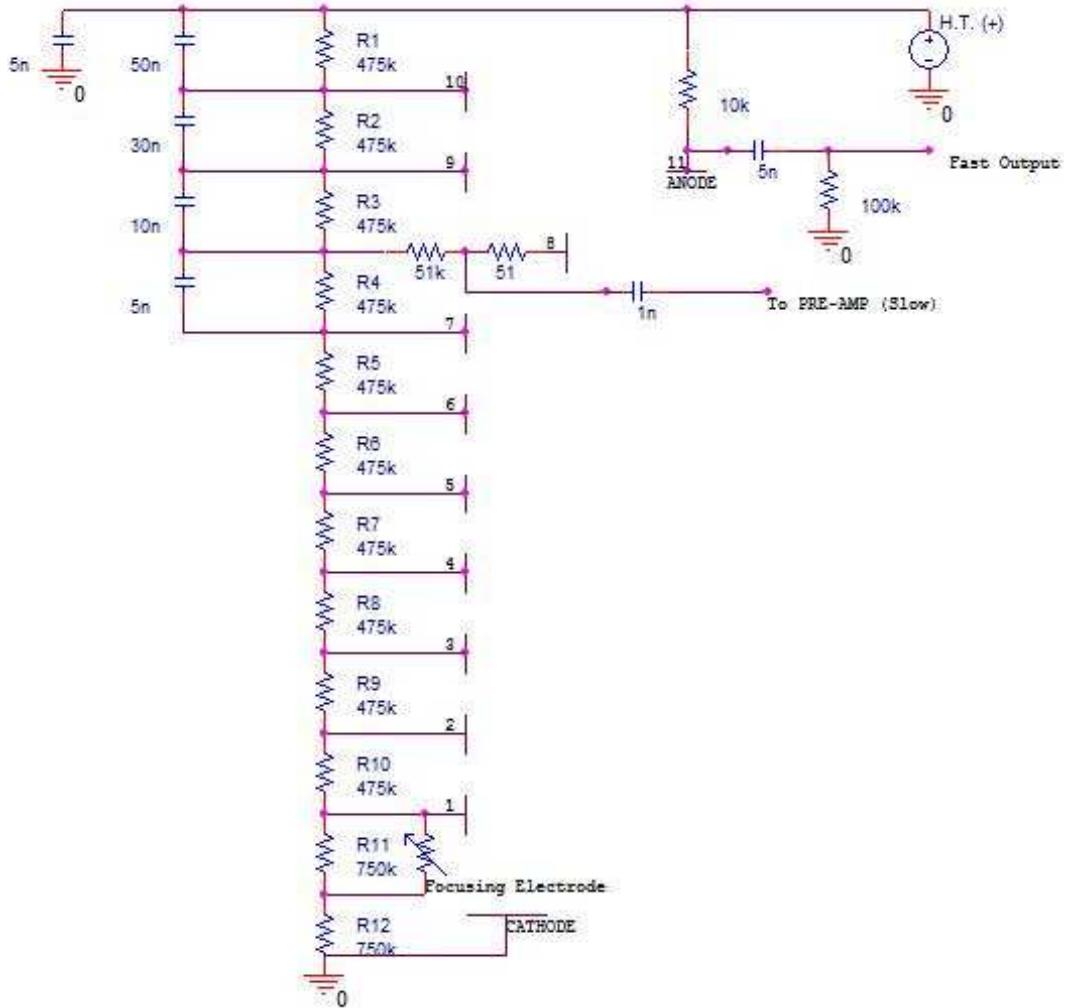


Figure 5.9: Electronics diagram of the PMT bases.

The signals from each of the PMTs were fed through the linear amplifier and then to a summing amplifier. A multi-channel analyzer (MCA) was used as a monitor to

adjust the gain on each signal such that they have the same gain. The NaI spectra after the gain adjustment, which was recorded by the MCA in a Computer Automated Measurement and Control (CAMAC) system, is shown in figure 5.10. The four spectra were summed together to get the annulus spectrum. The summed signal was fed into a single channel analyser (SCA) that generate a logic signal when the height of the pulse is in the 1274 keV peak. This logic signal was put into coincidence (AND) with the 511 keV from the back PMT to generate the annulus and back PMT trigger. Due to the long time constant of the pulses pil-up was observed from this setup when operated with a 250 kBq ^{22}Na source. It was replaced by the fast electronics, which does not sum the pulses from different crystal and has shorter pulses. The pile-up was reduced by a factor of 4.

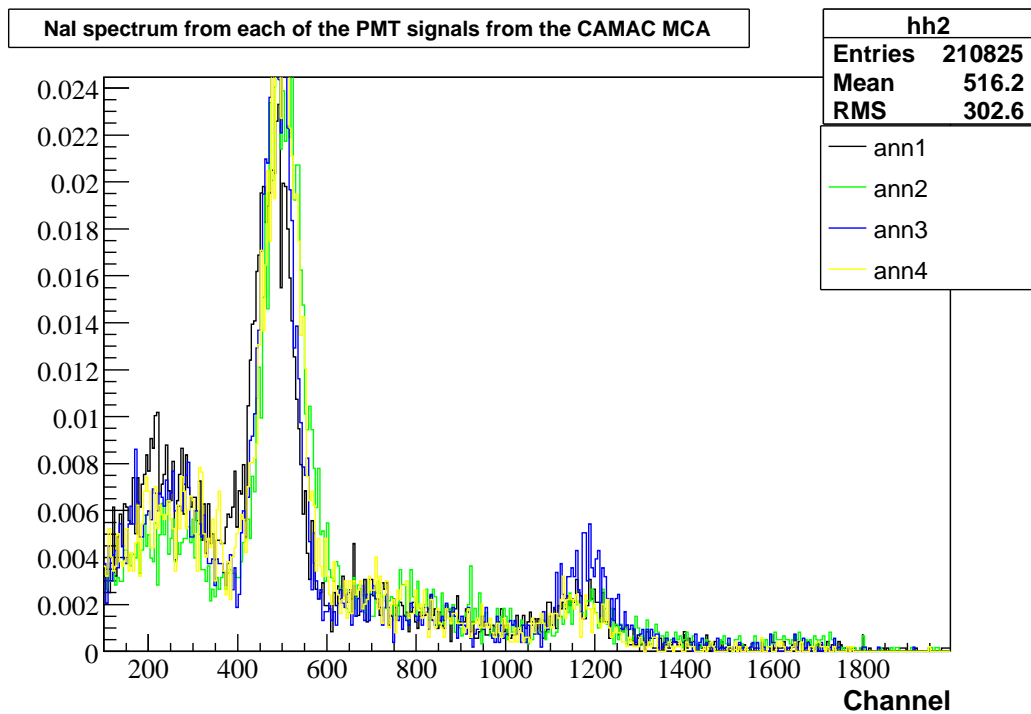


Figure 5.10: NaI spectrum recorded with the CAMAC MCA. The gain on each PMT was adjusted such that all the pulses line up with each other.

5.4 Fast Electronics

The fast electronics use the fast signal from the four annulus PMT bases. The fast signal is obtained from the anode directly without preamplification (see figure 5.9). The signals were put into the amplifier then into the discriminators, which produce logic pulse whenever the energy deposition in the NaI crystal is greater than 511 keV peak. These logic pulses were then put into an OR gate. The output from the OR gate is put into coincidence with the back NaI PMT to create the annulus and back PMT tag. This tag and the DEAP-1 trigger formed a global trigger. The logic diagram is shown in figure 5.11. The electronics diagram with gate width and

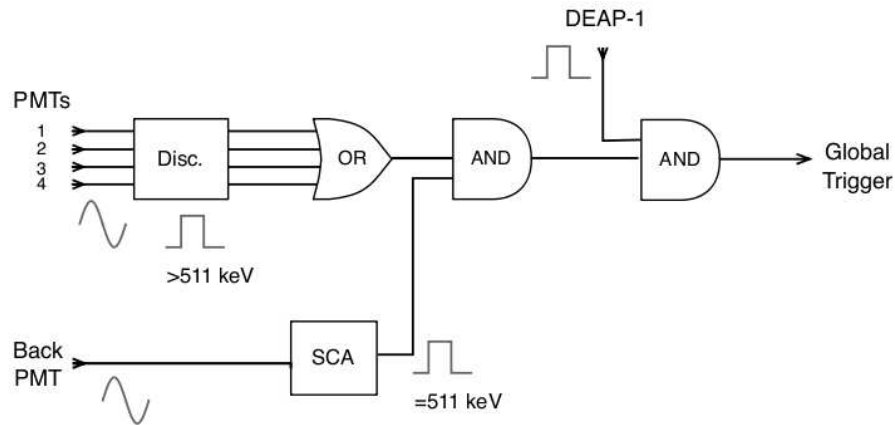


Figure 5.11: The logic diagram for the triple coincidence gamma calibration with the fast electronics.

components are shown below in figure 5.12. Figure 5.13 shows how the coincidence tag is created from DEAP-1 trigger and tag trigger.

From the previously mentioned electronics setup we find the optimum position by varying the source position until the coincident rate is maximized. The data and the DEAP-1 Monte Carlo seems to agree on the optimum position (see figure 5.14) , although there are still issues with the Monte Carlo.

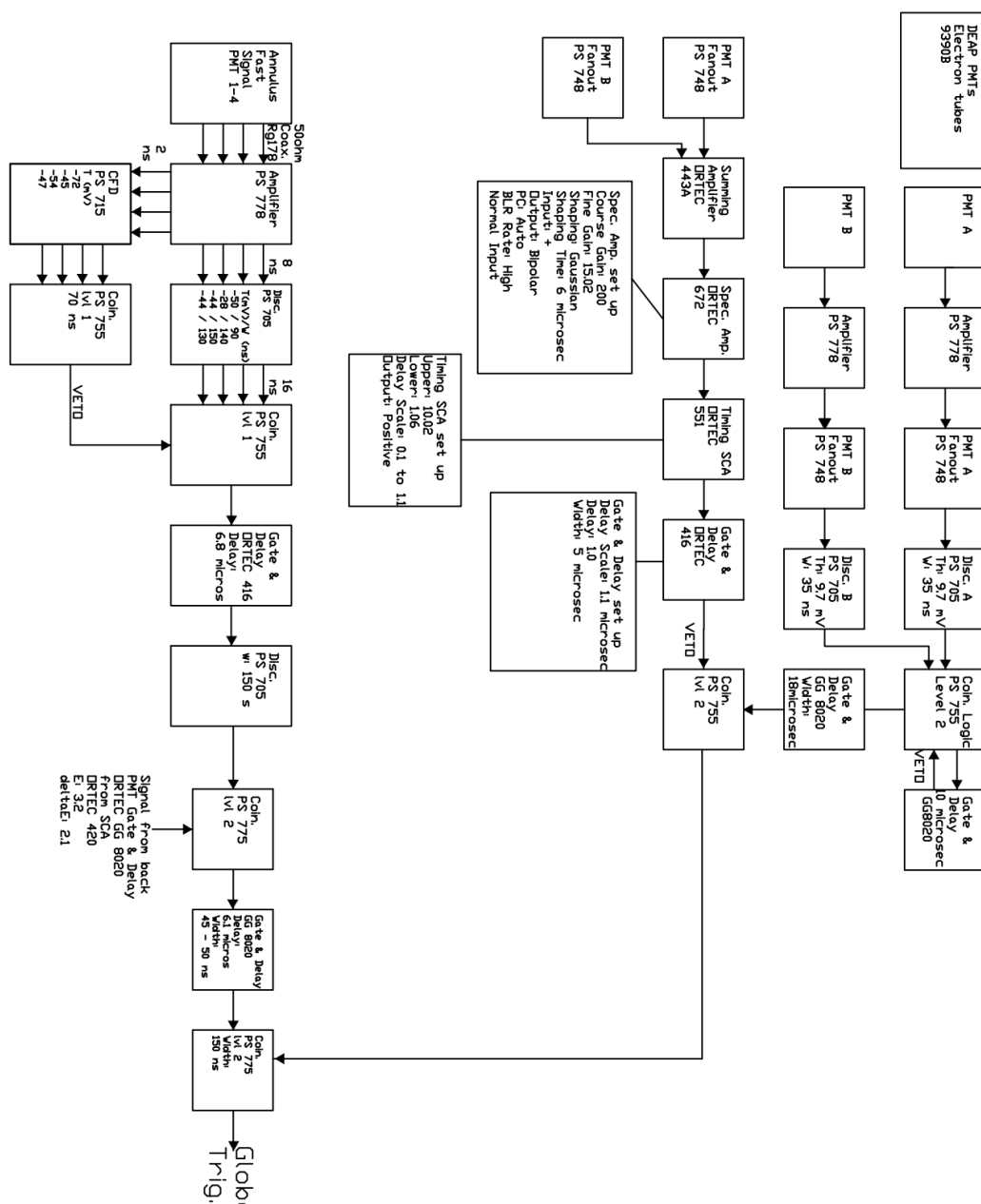


Figure 5.12: The electronics diagram of the triple coincidence gamma calibration. This diagram includes the setup of each component. The signals from the DEAP-1 PMTs were sent to the fan out unit via the amplifier. From the fan out unit, the delay veto trigger was created to prevent the trigger from re-triggering itself. The PMTs' signals were summed and sent through the SCA to create a veto signal against high energy events. The four signals from the annulus were amplified and sent through the discriminator to filter signals with energies above 511 keV, then then sent to the coincidence (level 1) unit to create a logic signal. The annulus signal from the coincidence box was sent to another coincidence (level 2) unit with the 511 keV signal from the back NaI PMT to create the tag signal. This tag signal and the DEAP-1 trigger formed the global trigger.

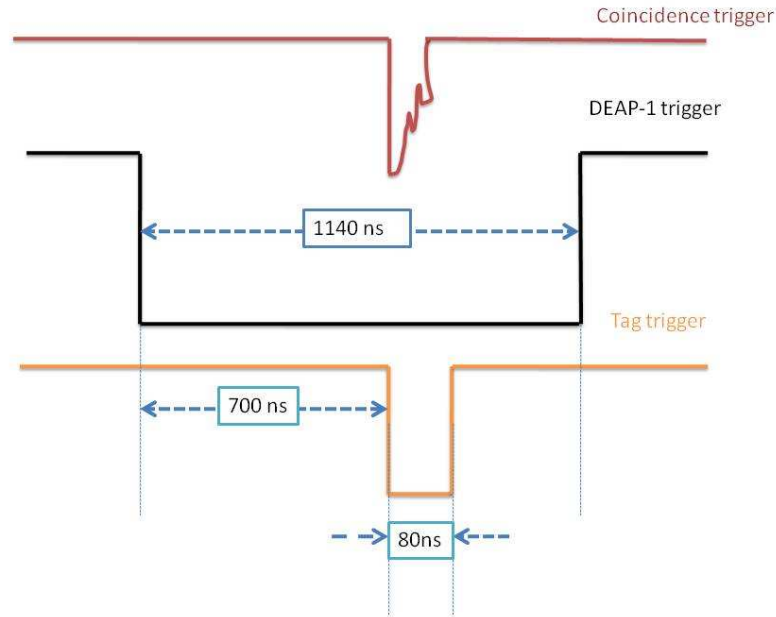


Figure 5.13: Diagram shows how the coincidence trigger is generated from the tag trigger and DEAP-1 trigger. Tag trigger refers to either the annulus and back PMT coincidence trigger (at Queen's University) and the back PMT coincidence trigger (at SNOLAB).

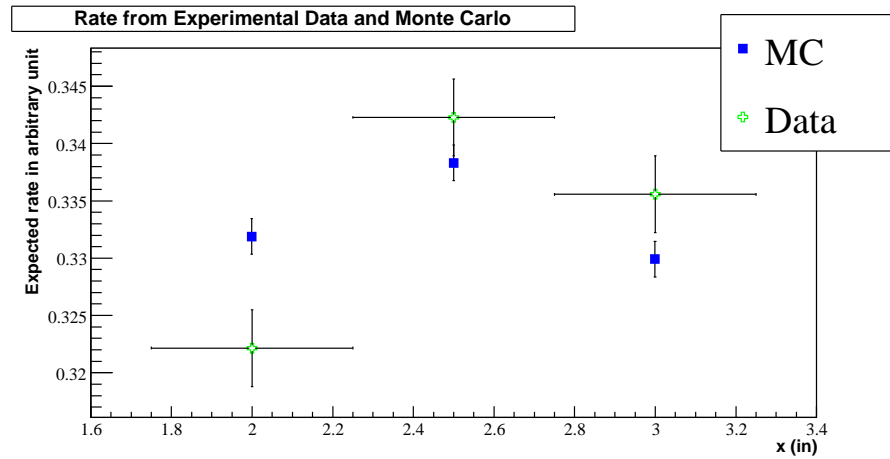


Figure 5.14: Comparison between expected rate from GEANT4 Monte Carlo and data rate at various positions. The MC and data agreed on the optimized source location.

The optimum position did not agree with what was predicted by the solid angle. This discrepancy occurs because the effective geometry of the annulus does not take into account factors such as the mean free path, scattering, etc. The configuration shown in figure 5.15 is the geometry of the triple coincidence gamma calibration at Queen's University.

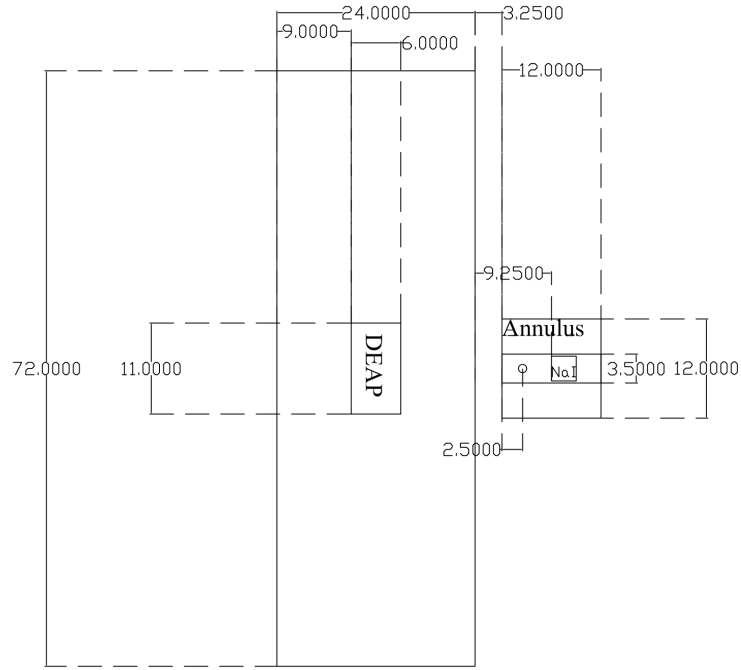


Figure 5.15: The triple coincidence gamma calibration geometry at Queen's University. The source is located 2.5" from the opening end of the annulus.

5.4.1 The Muon Veto Setup

One of the problematic backgrounds for DEAP-1 at Queen's University is the muon-induced neutron from spallation of nuclei. The cosmogenic muons are very energetic ($\sim\text{GeV}$) and could break nuclei apart. This process creates neutrons, which may

generate nuclear recoil events in DEAP-1. There are several reasons that muon-induced neutrons raise such a large concern [35]:

- The muon-induced neutrons have an energy spectrum that extends to the GeV range. These neutrons can travel very far and it is difficult to shield them from the detector.
- They transfer larger energies to nuclear recoils and make them visible in dark matter detector, while the room neutrons (neutrons from construction material/radioactivity from earth crust) have insufficient energy to reach the detector threshold.

There are two ways of shielding against muons. One way is to passively shield the detector. This is not very feasible on the surface run at Queen's University but it is done automatically underground at SNOLAB. The other way is to use active muon veto system, which was implemented at Queen's University.

One of the main concerns is the neutron spallation in lead shielding of the annulus. Figure 5.16 shows various background runs with the annulus in the PSD position. It can be seen that the background rate from these runs is 10 ± 1 mHz, which is larger than the standard background run (4.61 ± 0.17 mHz) by over a factor of two. Data from run 393, 394, and 395 were designed to estimate the neutron backgrounds that are related to the annulus. These runs used the standard DEAP-1 trigger in coincidence with the annulus trigger. The F_{prompt} distribution of these events in the ROI (120–240 PE) of these runs is shown in figure 5.17. There are 9 events in the high F_{prompt} (0.70–1.00) region. These events are nuclear recoil events and it is likely that they are from neutrons that are associated with the annulus. The rate of events in the WIMP window is 0.28 ± 0.22 mHz.

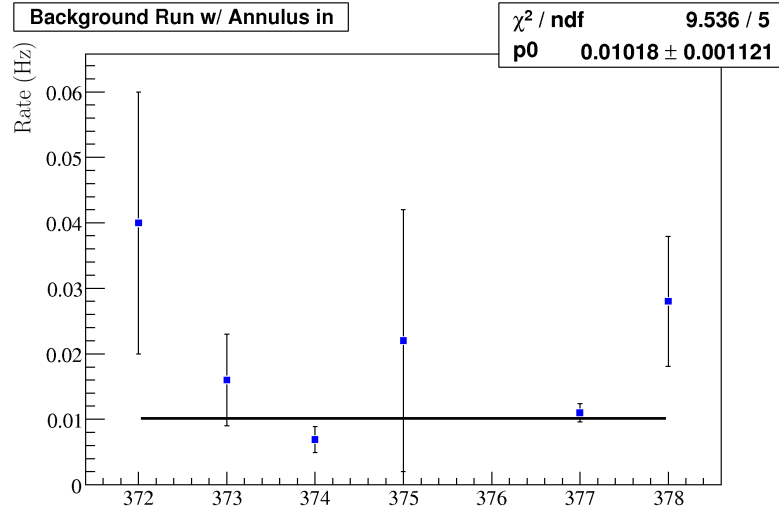


Figure 5.16: Rate of the various background runs with the annulus in the same position as the PSD runs.

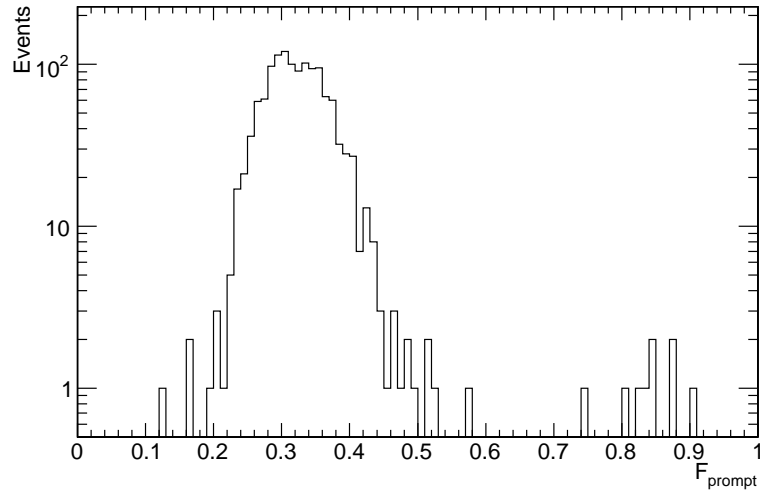


Figure 5.17: Region of interest (120–240 PE) of run 393, 394 and 395: From the figure it can be seen that there are 9 high F_{prompt} events (0.7–1.0). These events are inside the WIMP window.

The active veto was implemented by removing events, where a lot of energy was deposited in the annulus. This was accomplished by feeding the signal from the amplifier PS 778 into the constant fraction discriminator PS 715. A logic signal is generated whenever the energy is greater than 1274 keV peak. This logic signal is used as a veto in the coincidence box PS 755 (see figure 5.12). The system vetoed about 25 events per second.

5.5 DEAP-1 SCA Cut

Since our energy ROI is from 20-40 keV (electron recoil) and we are limited by the data read out rate, it is possible to speed up the data taking rate by using the SCA to cut out the higher energy region. The electronics set up is shown in figure 5.12.

5.6 Underground Electronics

The data in the background runs suggested that the background rate at SNOLAB after an appropriate data cleaning cut is about 0.6 mHz (see figure 4.8 in section 4.5). We believe that for the given background rate it is sufficient just to have a single PMT mounted with NaI crystal and only use the two 511 keV γ s from the annihilation process as the source. This is because it is likely that we are limited by the internal background of DEAP-1 at SNOLAB and not by muons or neutrons. We do not expect correlated backgrounds between the tag and the argon. The geometry of the setup is shown below in figure 5.18

To maximize the trigger rate, we calculated the optimum position of PMT based

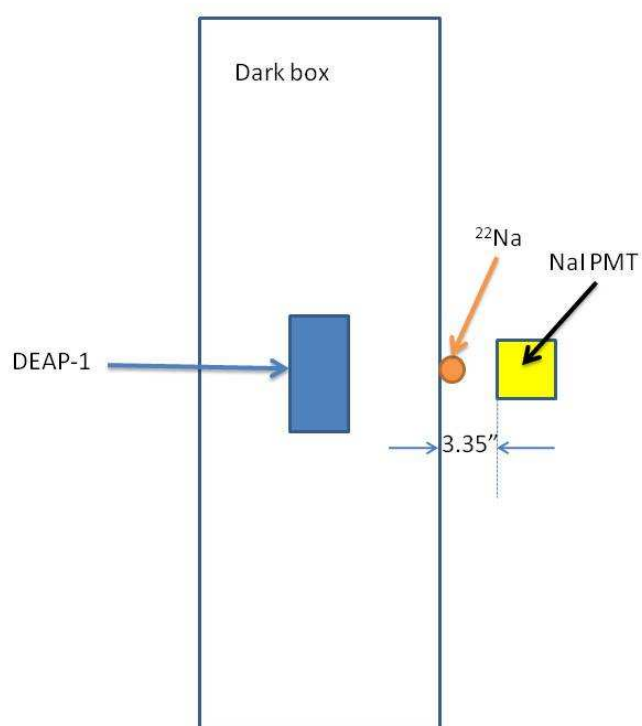


Figure 5.18: The double coincidence gamma calibration geometry at SNOLAB.

on the solid angle. The calculation was made such that the entire solid angle of DEAP-1 detector was covered by the back PMT solid angle. The calculation predicted that the back PMT should be 3.5" from the source. However, we should also take the mean free path of 511 keV γ in NaI crystal into account. The total mass attenuation coefficient of 511 keV γ in NaI is $9.33 \times 10^{-2} \text{ cm}^2/\text{g}$ and it is $5.11 \times 10^{-2} \text{ cm}^2/\text{g}$ for 1274 keV γ [36]. The NaI crystal has the density of 3.67 g/cm^3 . Therefore, the mean free path of the γ s in the NaI crystal are 2.92 cm and 5.33 cm for the 511 keV and 1274 keV γ respectively and added this distance to the PMT position. The other issue with the source is that we do not know the location of the source inside the PET capsule, which gives us large uncertainties on the exact position. Based on the solid angle calculation and on the assumption that the source is exactly in the middle of the 1.5" capsule, the back PMT should be placed approximately 3.1" from the darkbox. In practice the optimized location depends on the type of oscilloscope settings (used to digitized the signal) used for that particular run.

The setup of the NaI PMT electronics is almost identical to the setup used at Queen's with a few minor changes. ORTEC 420 Spec. Amp. was replaced by a newer ORTEC 672 amplifier and we used the fast output from the PMT base. The electronics diagram is shown in figure 5.19.

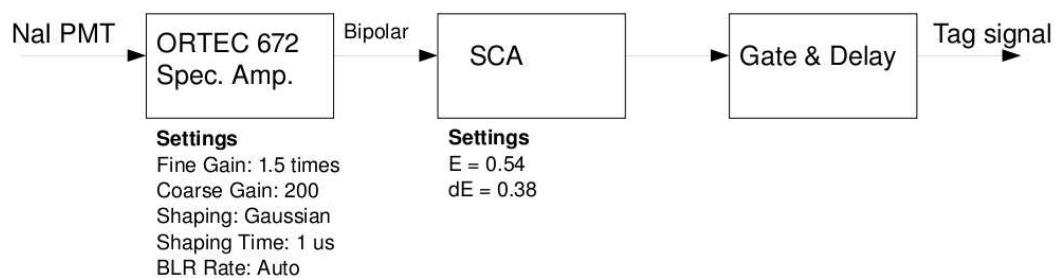


Figure 5.19: The underground NaI PMT tag electronics diagram.

Chapter 6

Result and Analysis

6.1 Understanding Pile-up Events

It was already stated that one of the main objective of DEAP-1 is to demonstrate the discrimination power against the gamma and beta events required for DEAP/CLEAN-3600. To demonstrate the high-level PSD, the random coincidence between the γ -tag and neutron background in DEAP-1 becomes important. The rate of neutron pile-up during the gamma calibration run, $R_{pile-up}$ is calculated using equation 6.1,

$$R_{pile-up} = R_{BackPMT} \cdot R_n \cdot (\Delta t_1 + \Delta t_2), \quad (6.1)$$

where $R_{BackPMT}$ is the rate of the back PMT, R_n is the rate of neutron background¹ measured in DEAP-1, Δt_1 is the width of the back PMT logic signal, and Δt_2 is the width of DEAP-1 trigger logic signal respectively. The achievable PSD can be found by simply dividing $R_{pile-up}$ by the rate of data acquisition in the energy ROI, R_{ROI} . In the current gamma calibration setting, we can acquire data in the ROI at

¹Here we define “neutron” background to be any high- F_{prompt} background in DEAP-1.

80 Hz and the high F_{prompt} background event rate in the ROI was measured to be 0.6 mHz. With the software cut on the timing window of 60 ns (see timing cut in section 6.2.1 for more detail), we calculated the expected PSD from equation 6.1 to be $\sim 3.6 \times 10^{-9}$ (see table 6.1 for variables used in the calculation). However, we found an event inside the WIMP window at PSD of 1.2×10^{-8} . According to the Poisson distribution (equation 6.2 [37]), we have a probability of about 24% of seeing one coincident neutron event for a given total number of events in the ROI.

$$P(r) = e^{-m} \frac{m^r}{r!}, \quad (6.2)$$

where $P(r)$ is the probability of seeing r events, $m (= np)$ is the expected number of seeing an event, n is the number of events, and p is the probability of seeing an event in WIMP window.

Table 6.1: Variables used for the pile-up prediction.

Variables	Values
R_{PMT} (Hz)	8800
R_{ROI} (Hz)	80
Δt_{sum} (ns)	60
R_n (mHz)	0.6

While it is possible to test this prediction by lengthening the gamma calibration run, it is very time consuming. One way to test the pile-up calculation is to increase the neutron background rate while running the gamma calibration. The SNO AmBe source O, which is a neutron source with a strength of about 100 μCi , was used in the calibration. The AmBe source is a mixture of an ^{241}Am and ^9Be neutron source. The α 's from ^{241}Am decay induce an the (α, n) reaction on ^9Be . Figure 6.1 shows the decay scheme of ^{241}Am - ^9Be . The source was placed on the right side of left stainless steel support and was shielded from the back PMT by a layer of plastic wood. After

the neutron source was in place, we first measured the in situ neutron background. The result of the measurement is shown in figure 6.2 and 6.3. From those two figures we calculate the rate of neutrons in the region of interest to be 48 ± 5 mHz.

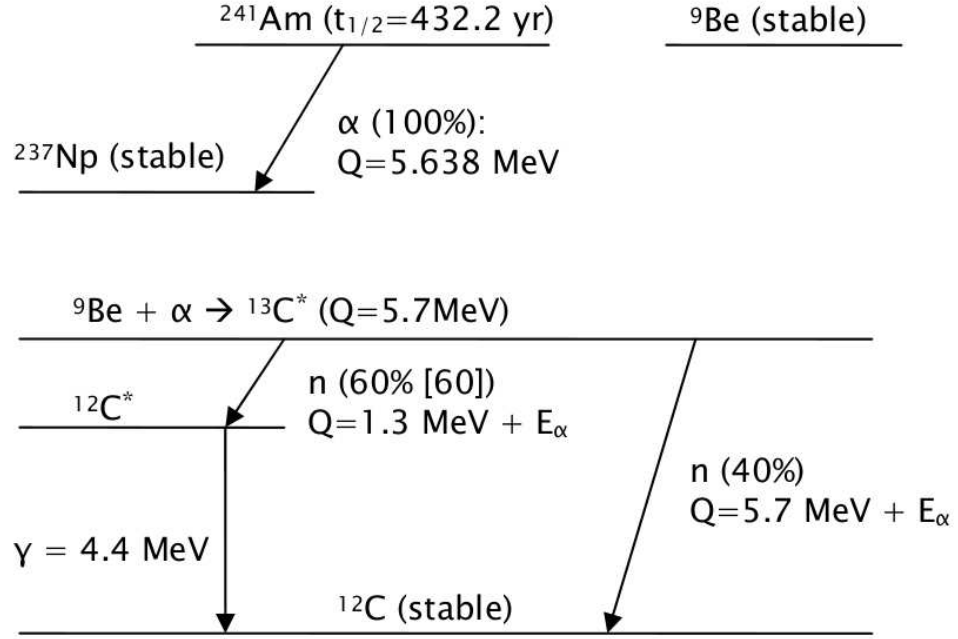


Figure 6.1: AmBe decay scheme. Figure from [23].

After we measured the neutron background with the AmBe source in place, we started a set of standard gamma calibration runs with the neutron source in the same position as in run 1711. The result from the set of runs is shown in figure 6.4. We found 9 high F_{prompt} events in the region of interest, which corresponds to the neutron pile-up rate of 0.3 ± 0.1 mHz. Using equation 6.1, we can calculate the expected neutron rate in the gamma calibration window. With the software window of 800 ns (Δt_{sum}) and the back PMT rate of 8880 Hz, we obtain 0.34 ± 0.04 mHz, which agrees with the experimental value. Table 6.2 shows all the variables that

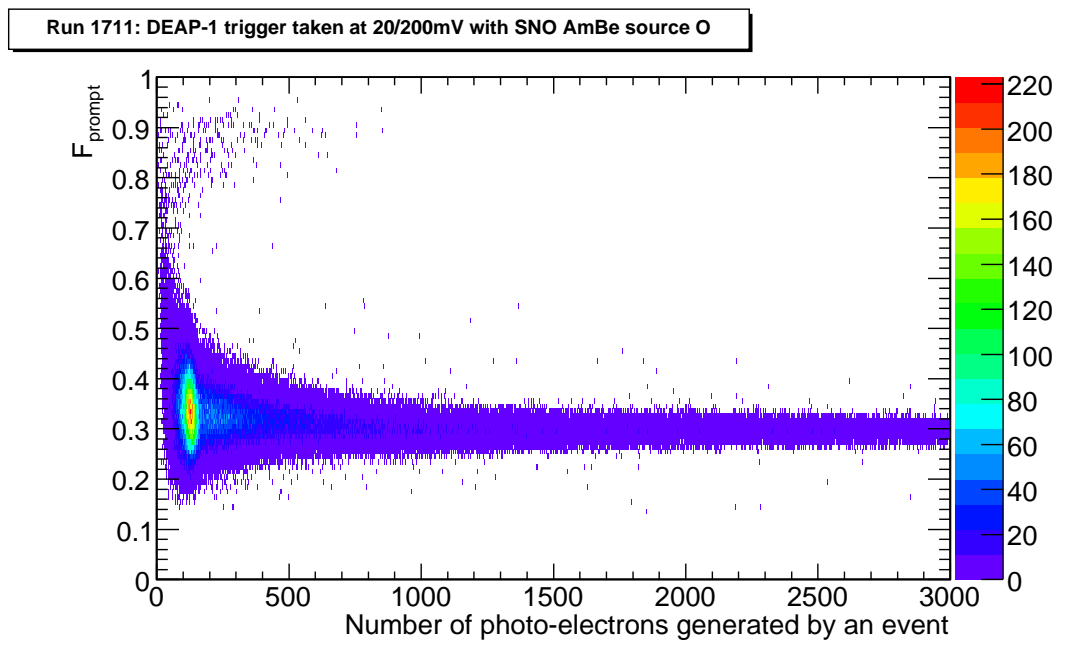


Figure 6.2: Run 1711 with SNO AmBe source O, refer to text for configuration.

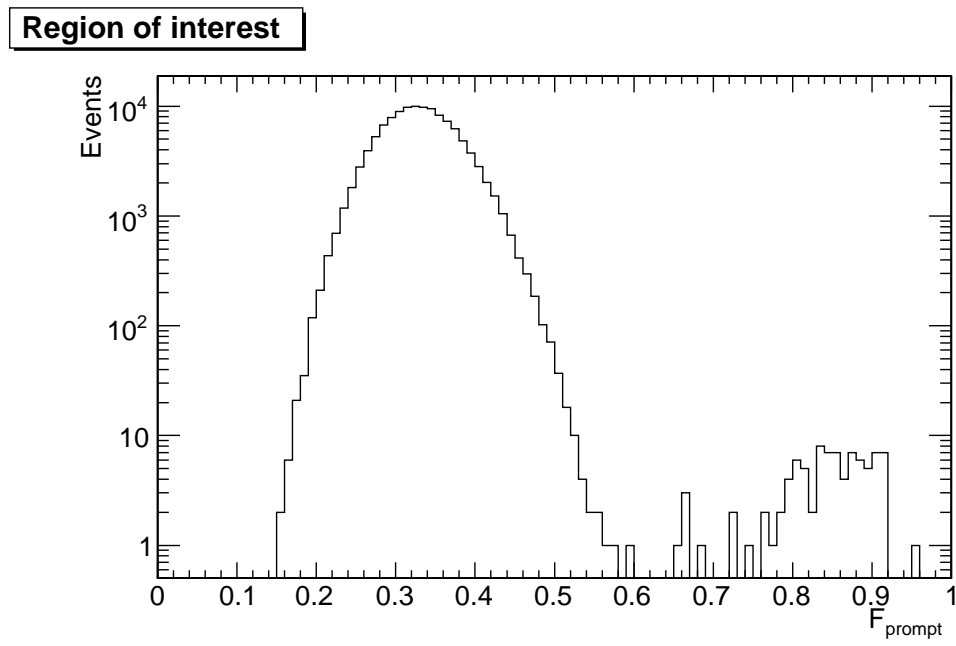


Figure 6.3: Run 1711 energy ROI. There are many events in the high F_{prompt} part from the neutron source.

were used for this calculation. Table 6.3 compares the result from the test with the predicted value from equation 6.1. We also checked all the pulses of the high F_{prompt} events in the ROI to make sure that they look like nuclear recoils. An example of these pulses is shown in figure 6.5.

Table 6.2: Variables used for the pile-up calculation test.

Variable	Values
R_{PMT} (Hz)	8900
Δt_{sum} (ns)	800
R_n (mHz)	48 ± 5

Table 6.3: Comparing the predicted neutron pile-up rate and the calibration data from run 1720–1725.

Predicted neutron pile-up rate (Hz)	Experimental (Hz)
0.34 ± 0.04	0.3 ± 0.1 mHz

6.2 Cuts and Correction

Various software cuts are applied to reduce the amount of unwanted data. These cuts required that each pulse contains enough PEs for the analysis, the DEAP-1 PMTs must trigger within a preset time between each other, the location of the event must be in the detector, etc.

6.2.1 Timing Cuts

In DEAP-1, Edge0 and Edge1 represent the zero crossing time of the signal of PMT A and PMT B relative to the external trigger. It is used in the PSD run to select the γ event, which is generated by the ^{22}Na . An example of this is shown in run 1488

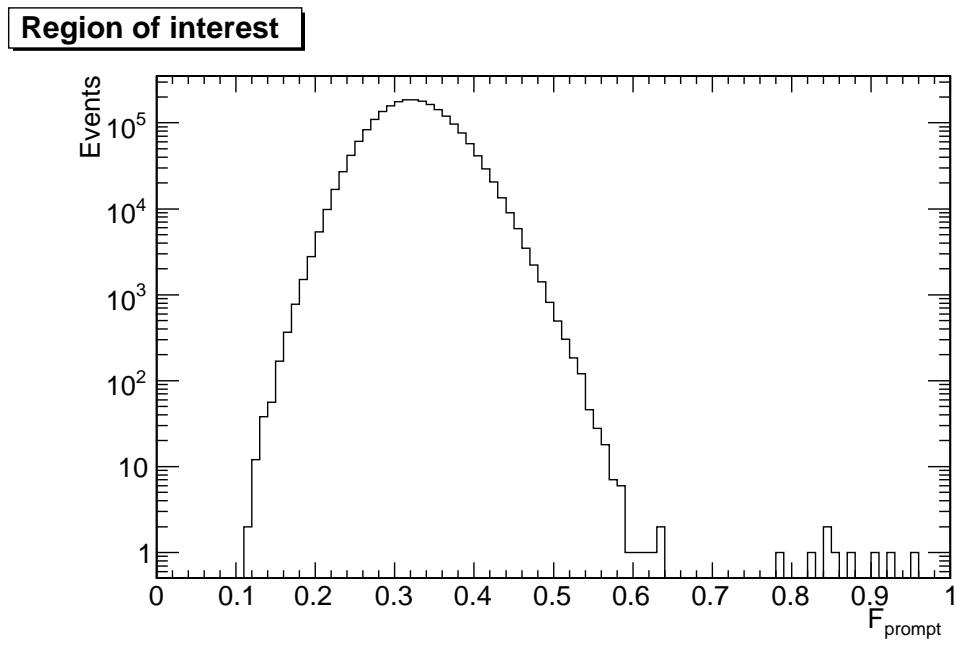


Figure 6.4: Run 1720–1725 were taken with both AmBe source and Na-22 source with standard gamma calibration trigger and a software window width of 800 ns.

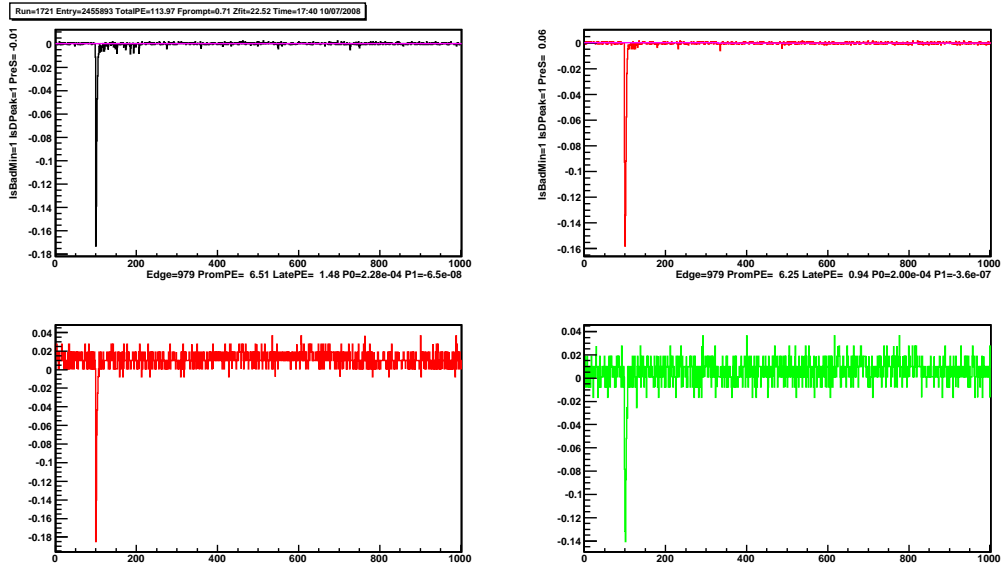


Figure 6.5: A high F_{prompt} event in the ROI from run 1721. The pulse is dominated by the prompt light, which is a characteristic of a nuclear recoil event. There are 4 different PMT channels for this event (shown in different colors). The 4 channels are high gain and low gain of PMT A and PMT B.

(see fig 6.6), where over 80% of the signal lies within 2σ of the peak's mean. Thus the Edge0 cut was set to be $\pm 2\sigma$ from the peak.

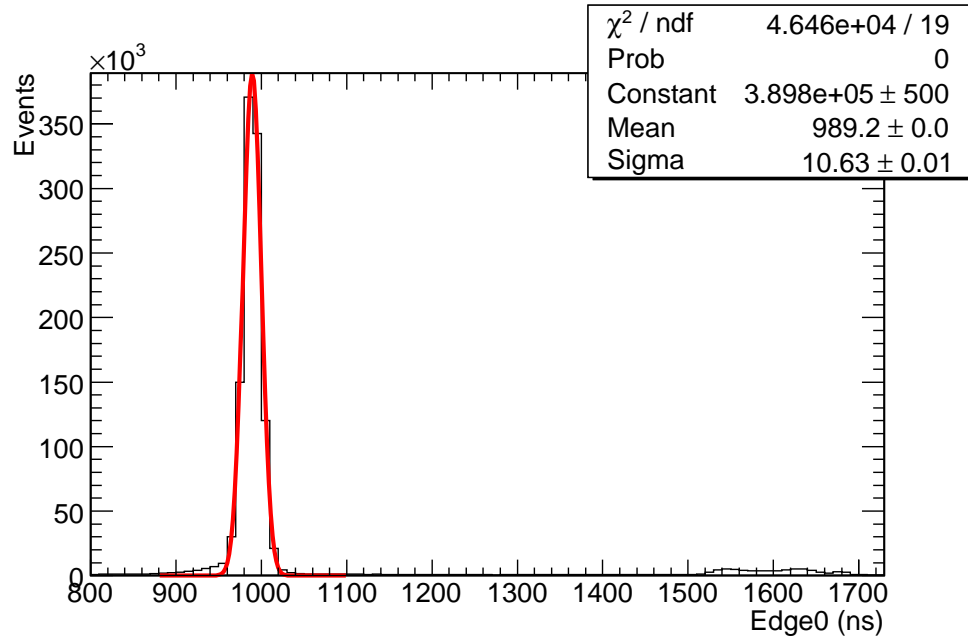


Figure 6.6: The zero crossing time of PMT 1, with gaussian fit to the peak in red.

6.2.2 PE Correction and Cuts

In DEAP-1, we selected the energy region of interest to be between 120–240 PE. From the surface data (see [23]), it can be seen that DEAP-1 PE yield for DEAP-1 is about 2.8 PE/keV, this makes our ROI window spans the range of $\sim 40 - 80$ keV. During the runs on surface, the data acquisition rate was limited by the triple coincidence rate (see appendix A), which is restricted by the geometry of the annulus and the source strength. When the detector was moved underground, however, there is a possibility of increasing the data acquisition rate by changing the digitization setup on the scope

(at SNOLAB without that annulus, the rate is so high that we are limited by the DAQ itself). It was first proposed to change the digitization intervals from 1 ns to 10 ns, which should allow us to take data at 10 times higher rate. Later though, it was found that by changing the time bin, the F_{prompt} resolution got worse. It was then suggested that we could increase the resolution by changing the sensitivity from 50 mV per division to 20 mV per division, which did make the F_{prompt} distribution narrower. However, it was still wide compared to the 1 ns run on surface. Later in this section we will discuss this subject in more detail.

The wider F_{prompt} distribution is not the only effect caused by the change of electronics. When comparing the 10 ns time bin runs from underground to the 1 ns surface runs, there is a discrepancy between the light yield of the detector. Since the only change made was the electronic digitization of the scope, the actual light yield should remain the same. It was just not taken into account properly. We should be able to make a correction on the PE by comparing the position of the ^{22}Na peak and make an adjustment so that the peak from the runs with 10 ns time bin would line up with the 1 ns. An example of this correction is shown in runs 1488–1517, where we pick run 1523 as its PE calibration. The ^{22}Na peak of run 1523 is shown in figure 6.7. The peak corresponds to the light yield of 2.24 PE/keV. If we compare this light yield of 2.8 PE/keV from the 1 ns run, we can use the ratio between these two numbers to scale the PE yield from runs 1488–1517 correctly.

After the PE yield correction, the comparison between the data with and without correction are plotted with the 1 ns surface runs (see fig 6.8). It can be seen from figure 6.8 that the F_{prompt} distribution of the 10 ns with 50/500 mV/div. setting is much broader than the 1 ns surface data. The 20/200 mV/div. scope setting at 10

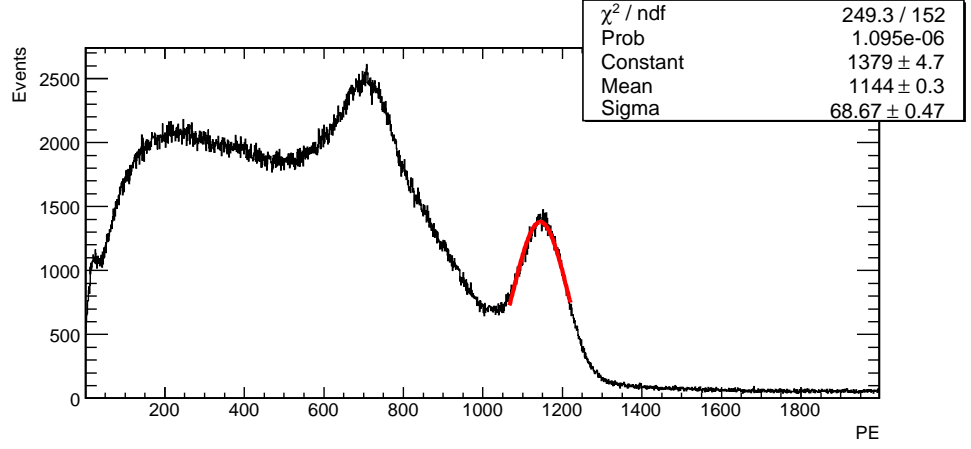


Figure 6.7: The 511 keV peak position from run 1523 (see appendix A for more detail).

ns also shows similar behavior (see fig 6.9). The collaboration is convinced that the poorer resolution arises from the increase in bit noise caused by the different setting. Since the number of bits on the memory of the scope is fixed, as the setting increases each bit corresponds to a larger value, which amplify the effect of bit noise. It was decided that the 10 ns data will not be used for the standard analysis since their F_{prompt} distributions are too wide.

6.2.3 Stability of the high F_{prompt} Background

Understanding high F_{prompt} background (0.7–1.0) is DEAP-1 analysis highest priority since this background governs the detector sensitivity to WIMPs and achievable PSD. The background rate seems to be position dependent. Z_{fit} is event reconstruction based on the number of PE in each PMT given by [38]:

$$Z_{fit} = \frac{-35.2 \cdot TotalPE_A + 35.2 \cdot TotalPE_B}{TotalPE_A + TotalPE_B}, \quad (6.3)$$

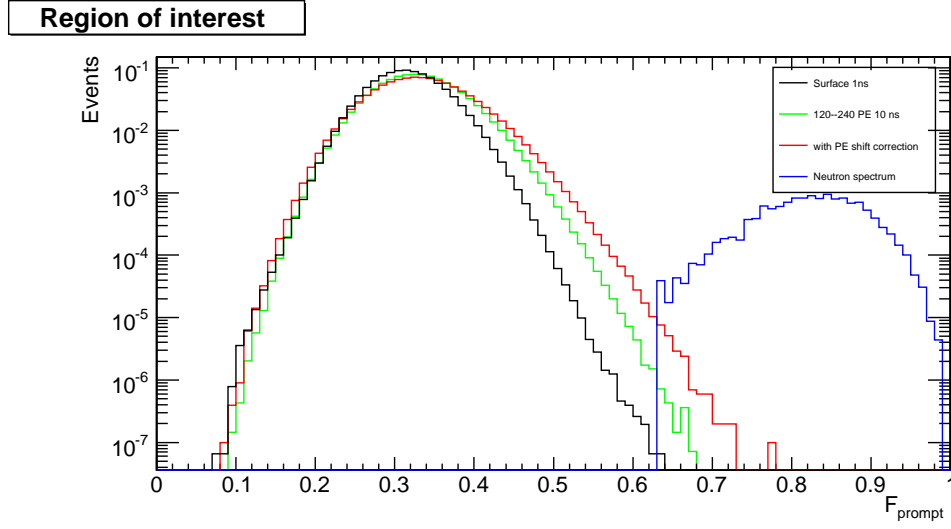


Figure 6.8: Comparing the F_{prompt} plots with and without correction in the ROI from runs 1488-1517 (10 ns with 50/500 mV/div. setting) with the 1 ns data from surface. Figure is overlaid with the neutron spectrum from run 316.

where 35.2 cm is the distance from the PMTs to the centre of the detector, and $TotalPE_{A,B}$ are the total PEs collected by PMT A and PMT B, respectively.

Figure 6.10 was generated to show the variation of high F_{prompt} background in the ROI over four sets of background runs. It can be seen that there are two distinct peaks located at Z_{fit} value of about -6 cm and 22 cm, throughout all the runs. There is no distinctive difference between these runs. where 35.2 cm is the distance from the PMTs to the centre of the detector, and $TotalPE_{A,B}$ are the total PEs collected by PMT A and PMT B, respectively.

The stability of these backgrounds are shown in figure 6.11 as function of time in month of 2008.

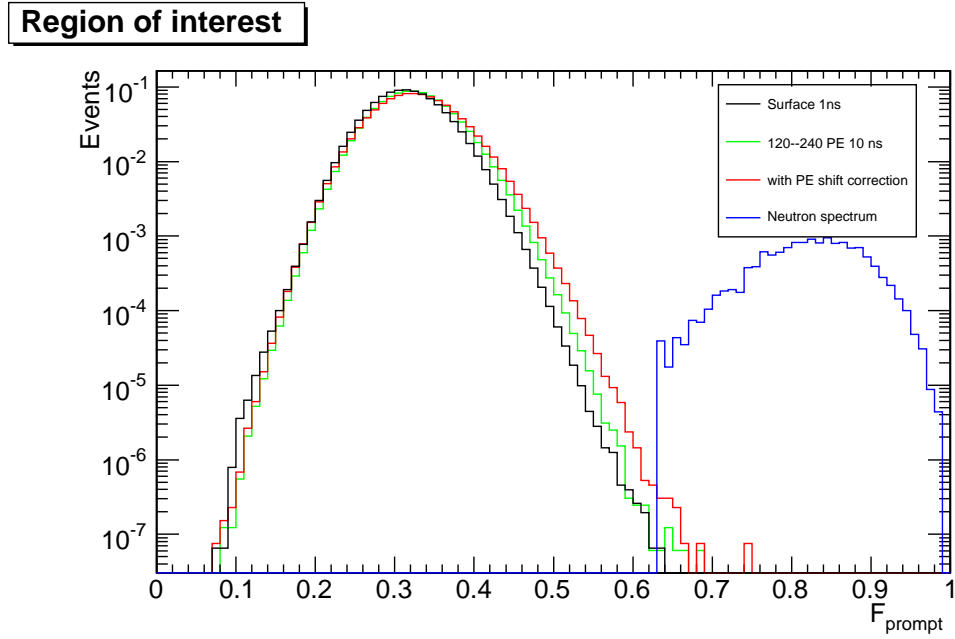


Figure 6.9: Comparing the F_{prompt} plots with and without correction in the ROI from runs 1622–1651 (see appendix A for more detail.) with the 1 ns data from surface. Figure is overlaid with neutron spectrum from run 316.

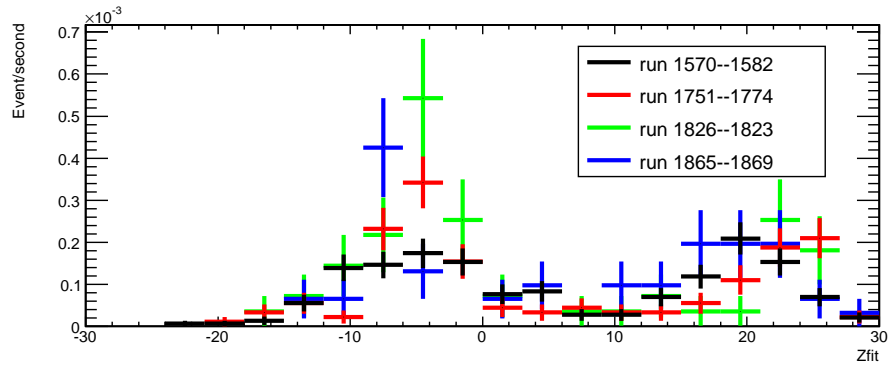


Figure 6.10: Comparing the high F_{prompt} events in the ROI from various background runs. All the runs seems to share similar features.

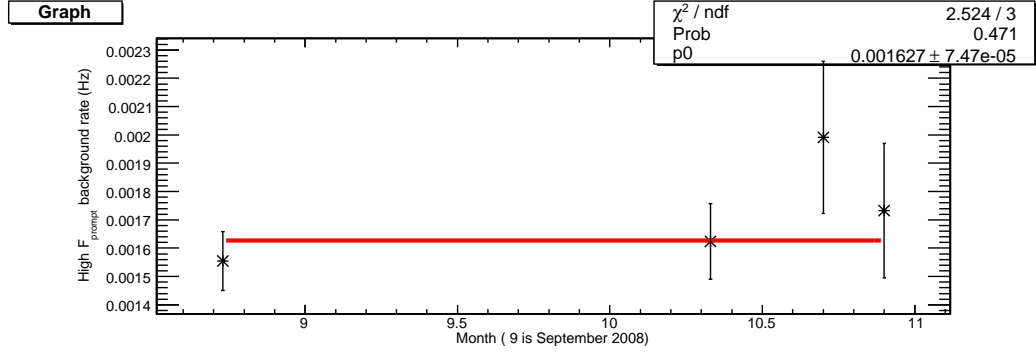


Figure 6.11: The stability of high F_{prompt} rate without Z_{fit} cut in the energy ROI from background runs over several months.

6.2.4 Z_{fit} Cut and PSD

Z_{fit} is one of the parameters that was used in DEAP-1 data cleaning cuts. Figure 6.12 compares the background rate in the WIMP window from SNOLAB and Queen's University. From the figure it can be seen that after the detector was moved underground, the background was substantially reduced. The majority of the background events at Queen's University are likely the Cherenkov radiation from muon interactions in the acrylic light guides; These events have been largely reduced due to the much lower muon rate at SNOLAB. Figure 6.10 gives us an important information about the background. It tells us that there are two distinct peaks, which remain at stable Z_{fit} positions. Since the PSD depends on the ratio between signal and background, this information could be used to select the ideal Z_{fit} cut. The ratio between the PSD data and the background was calculated and recorded in table 6.4 as a function of Z_{fit} width, where the cut is centered at the mean of the PSD data. The F_{prompt} window between 0.7 and 1.0 corresponds to 95% neutron survival probability.

The data from the in table are plotted and shown in figure 6.13. From the data

Table 6.4: The achievable PSD with $F_{prompt} = 0.7-1.0$, and the time required to reach that given PSD as a function of Z_{fit} width. The PSD was calculated using equation 6.1 divided by the R_{ROI} . From the data it can be seen that as the width of Z_{fit} cut increases, the data taking rate and the background rate increase. The live time can be converted to real time by dividing the live time by DEAP-1 data acquisition efficiency (~ 0.29 for the 2 ns run). The PSD shown in this table is the achievable PSD level with zero event at 90% confidence level calculated from equation 6.2.

Z_{fit} Width (cm)	Signal rate (Hz)	Background rate (mHz)	Achievable PSD ($\times 10^{-8}$)	Time required (livedays)
2	7.66	0.03	1.03	146.75
4	14.97	0.06	0.95	81.01
6	22.26	0.07	0.76	68.32
8	29.52	0.12	0.97	40.45
10	36.64	0.18	1.19	26.48
12	43.54	0.24	1.33	19.93
14	50.06	0.32	1.53	15.09
16	56.02	0.41	1.76	11.74
18	61.26	0.51	1.99	9.51
20	65.69	0.7	2.56	6.89
22	69.25	0.81	2.81	5.95
24	71.98	0.94	3.14	5.13
26	73.98	1.06	3.46	4.53
28	75.37	1.13	3.61	4.26
30	76.31	1.22	3.83	3.96
32	76.90	1.29	4.03	3.73
34	77.27	1.32	4.11	3.64
36	77.49	1.44	4.46	3.35
38	77.62	1.58	4.89	3.05

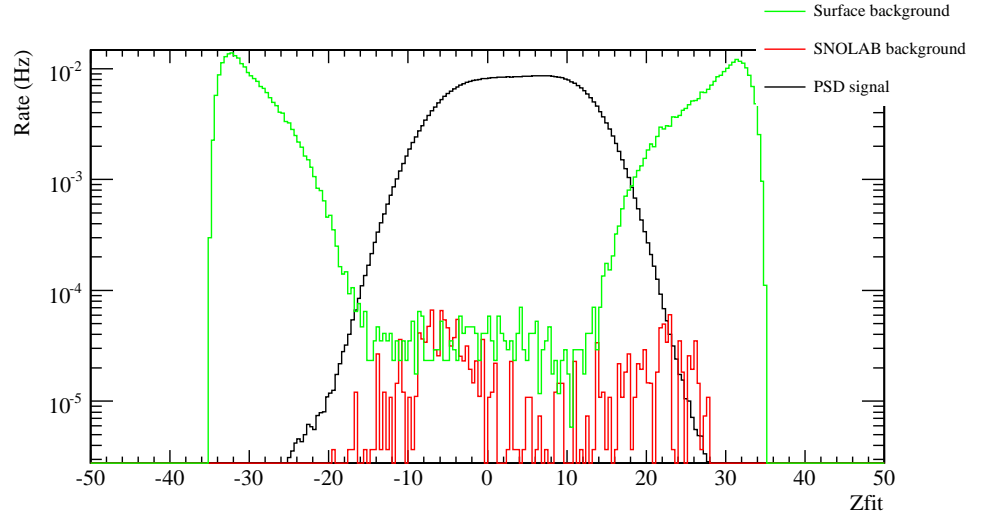


Figure 6.12: Comparison between the background rates as a function of Z_{fit} between data taken at SNOLAB and Queen’s University. The PSD data shown on the plot is normalized to have the same area as the background rate at Queen’s University.

it can be seen that at the current background rate the maximum possible PSD is 7.6×10^{-9} at Z_{fit} width of 6 cm and it will take 68 days of livetime or about 200 days of constant running (based on the data acquisition efficiency is 0.29).

6.3 Higher F_{prompt} Cut

From section 6.2.2, it can be seen that the 10 ns data set has a broader F_{prompt} distribution, which makes the data set inappropriate for DEAP-1 standard analysis, where the nuclear recoil window has F_{prompt} ranged from 0.7 to 1.0. It is possible, however, to make use of those data by trading off some neutron efficiency and select a narrower F_{prompt} window. Figure 6.14 shows the neutron survival probability as a function of the lower limit for the F_{prompt} cut; it was created by integrating the neutron spectrum

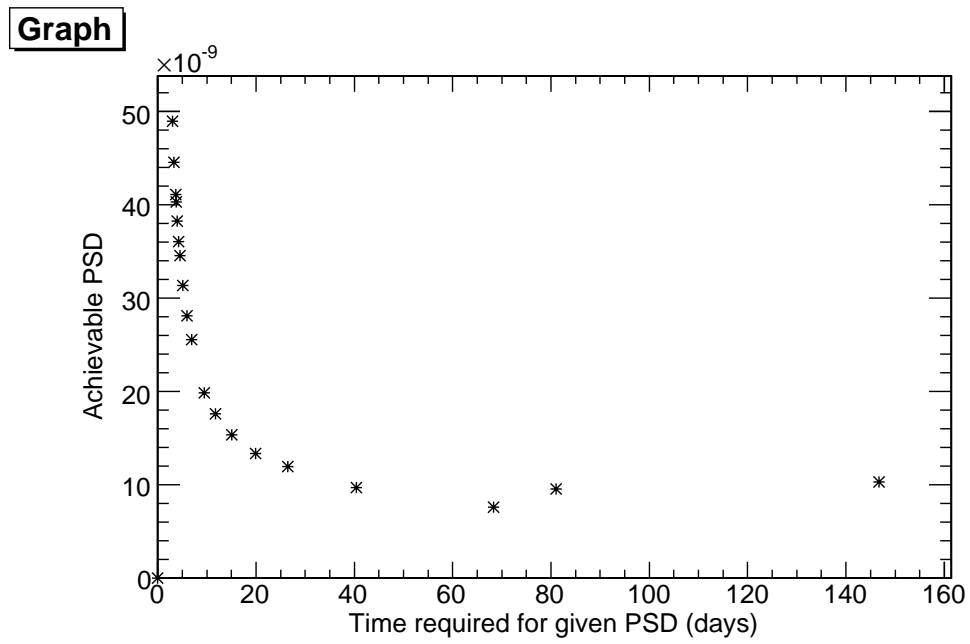


Figure 6.13: The achievable PSD and the time required to reach the given PSD. The time on the plot is given in live days, which can be converted to real time by dividing the live days by our daqq efficiency of 0.29. The PSD given on the plot represents the 90% probability of seeing zero events.

from the lower F_{prompt} cut to 1.0 and divided by the total number of neutron-like events from the spectrum. By narrowing the F_{prompt} window, the background rate and the neutron efficiency rate are reduced (see figure 6.15). For an F_{prompt} window of 0.85 to 1.0, the discrimination power demonstrated by the underground data is 1.13×10^{-8} . Figure 6.16 shows the ROI of the combined underground data and surface data. The combined PSD result is 9.6×10^{-9} . This F_{prompt} window corresponds to a neutron efficiency of $35.5 \pm 1.3 \%$.

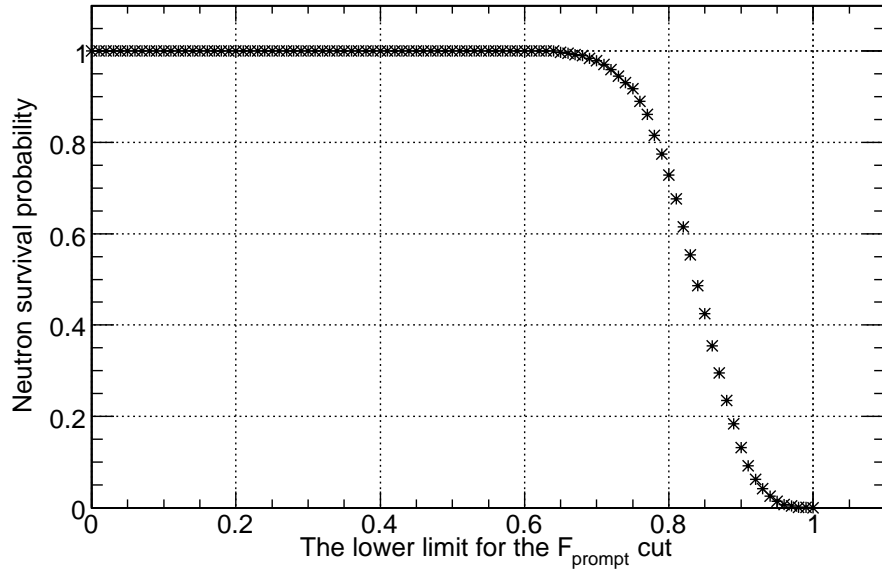


Figure 6.14: The neutron survival probability as a function of the lower F_{prompt} cut. The neutron spectrum was obtained from run 316.

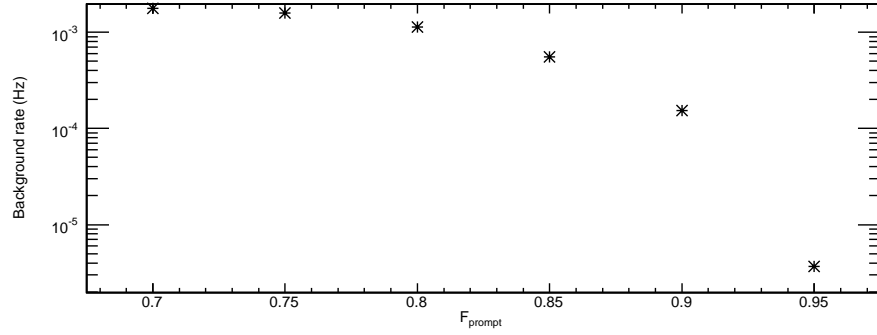


Figure 6.15: The background rate as a function of the lower F_{prompt} cut. The background rates do not include any Z_{fit} cut. By narrowing the F_{prompt} window, the background rate decreases.

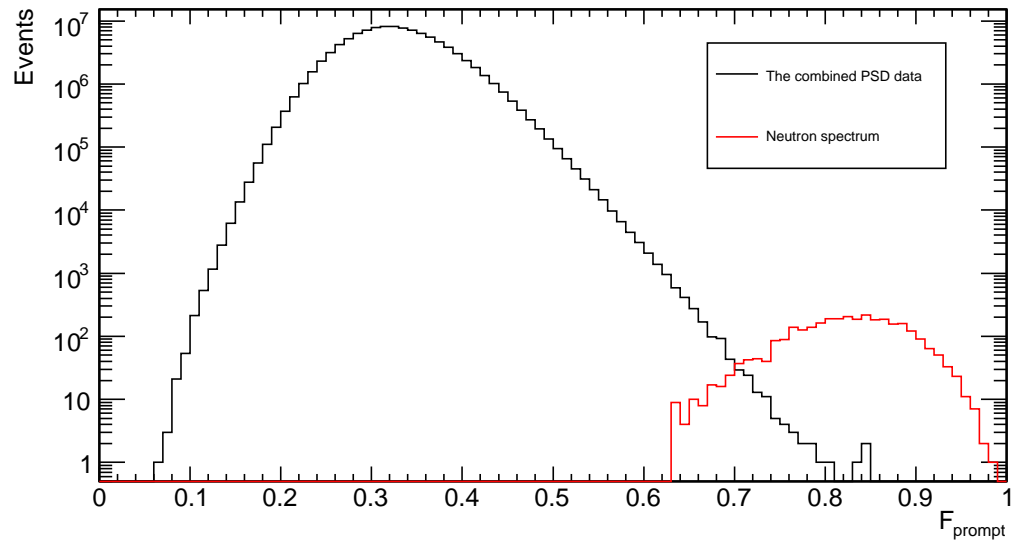


Figure 6.16: Combined underground and surface PSD data (see appendix A for more information). The PSD data are overlaid with the neutron background from run 316.

6.3.1 Achievable PSD with Higher F_{prompt} Cut

With the higher F_{prompt} cut (0.85–1.0), the same procedure used in section 6.2.4 can be applied to calculate the achievable PSD with this cut. Table 6.5 shows the PSD level with 90% confidence level, and the time required to reach the given PSD as a function of the Z_{fit} cut.

Table 6.5: The achievable PSD and the time required to reach that given PSD as a function of Z_{fit} width for the F_{prompt} window of 0.85–1.0. The achievable PSD refers to the best possible PSD we could reach based on the intrinsic PSD is perfect. The table shows the time requirement in both live time and real time. The PSD was calculated by using equation 6.1 divided by the signal rate, R_{ROI} . From the data it can be seen that as the width of Z_{fit} cut increases, the data taking rate and the background rate increase. The PSD shown in this table is the achievable PSD level with zero event at 90% confidence level calculated from equation 6.2.

Z_{fit} Width (cm)	Signal rate (Hz)	Background rate (mHz)	Achievable PSD $\times 10^{-9}$	Time required (live days)	Time req. (days)
2	7.7	0.01	3.22	468.7	1616.1
4	15.0	0.02	2.99	258.7	892.1
6	22.3	0.02	2.38	218.2	752.4
8	29.5	0.04	3.03	129.2	445.5
10	36.6	0.06	3.74	84.6	291.6
12	43.5	0.08	4.18	63.7	219.5
14	50.1	0.10	4.80	48.2	166.2
16	56.0	0.13	5.51	37.5	129.3
18	61.3	0.16	6.22	30.4	104.8
20	65.7	0.22	8.01	22.0	75.9
22	69.2	0.25	8.80	19.0	65.5
24	72.0	0.29	9.82	16.4	56.5
26	74.0	0.33	10.82	14.5	49.9
28	75.4	0.35	11.29	13.6	46.9
30	76.3	0.38	11.99	12.7	43.6
32	76.9	0.40	12.62	11.9	41.1
34	77.3	0.41	12.88	11.6	40.1
36	77.5	0.45	13.95	10.7	36.9
38	77.6	0.50	15.33	9.7	33.6

Chapter 7

Conclusion

7.1 Detector Performance

From figure 6.11, it can be seen that the high F_{prompt} background rates have remained relatively constant. The light-yield of the DEAP-1 detector at SNOLAB is ~ 2.8 PE/keV, which is the same as the light yield on surface [23]. Between all the PSD runs of various settings that were conducted underground (see appendix A for more details) we have collected 8.85×10^7 events. When combined with the PSD result from surface, the total number of events is 1.04×10^8 events. Figure 6.16 shows the combined data. From the combined data set the PSD level achieved is 9.64×10^{-9} , when selecting the F_{prompt} window between 0.85–1.0. This F_{prompt} window corresponds to a neutron efficiency of 35.5 ± 1.3 %. DEAP-1 has successfully demonstrated the PSD level required to discriminate against ^{39}Ar (see table). The PSD demonstration shows that DEAP-1 can discriminate against the internal ^{39}Ar background.

7.2 Achievable PSD

It was mentioned in section 6.3 that by narrowing the F_{prompt} window a higher PSD level can be achieved; this is because the background is lower (see figure 6.15) and we are less affected by the wide F_{prompt} distribution from the γ band. Figure 7.1 shows the achievable PSD plot with various F_{prompt} cuts, this is based on the assumption that the intrinsic PSD is perfect for a given F_{prompt} cut. The PSD level indicated with the arrow is 1.70×10^{-9} , which is lower than the PSD required for DEAP-3600 (1.8×10^{-9}). The time required to reach this PSD is 111 live days or 380 days of detector running. At this F_{prompt} the neutron efficiency is 9.1 ± 0.6 %. While it is possible to achieve the required PSD with this current background level, if the background level is reduced we could do it at a faster rate with higher efficiency for WIMPs.

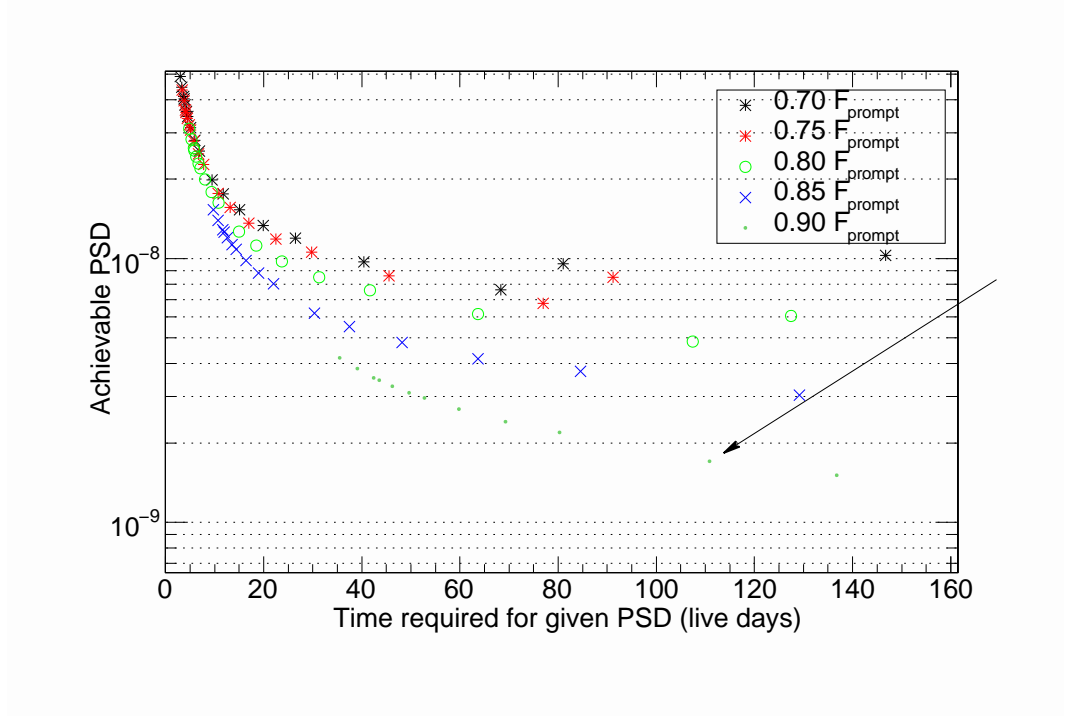


Figure 7.1: The achievable PSD and time it take to reach the given PSD. The time on the plot is given in live days, which can be converted to real time by dividing the live days by our data taking efficiency of 0.29. The PSD given on the plot represent the 90 % probability of seeing zero event. The PSD level indicated with the arrow is 1.70×10^{-9} , which is lower than the PSD level required by DEAP-3600 (1.8×10^{-9}). The time required to reach the given PSD is 111 live days or 380 days with the lower F_{prompt} cut of 0.90.

Bibliography

- [1] Steve Adams. *Relativity: An introduction to space-time physics*. CRC Press, 1997.
- [2] D. W. Sciama. *Modern cosmology and the dark matter problem*. Cambridge University Press, 1993.
- [3] K.C. Freeman. On the disks of spiral and so galaxies. *Astrophysical Journal*, 160:811–830, 1970.
- [4] G. Bertone, D. Hooper, and J. Silk. Particle dark matter: Evidence, candidates and constraints. *Phys. Rept.*, 405:279–390, 2005.
- [5] V. C. Rubin and W. Kent Jr. Ford. Rotation of Andromeda nebula from a spectroscopic survey of emission regions. *Astrophysical Journal*, 159:379, 1970.
- [6] J.P. Ostriker and P.J.E. Peebles. A numerical study of the stability of flattened galaxies: Or, can cold galaxies survive? *ApJ*, 186:467–480, 1973.
- [7] F. Zwicky. On the masses of nebulae and of clusters of nebulae. *Astrophys. J.*, 86:217–246, 1937.

- [8] C. L. Bennett et al. First year Wilkinson Microwave Anisotropy Probe (WMAP) observations: Preliminary maps and basic results. *Astrophys. J. Suppl.*, 148:1, 2003.
- [9] R. Schnee. Determination of WIMP mass (and cross section) with direct detection.
- [10] J. Angle et al. First results from the XENON10 dark matter experiment at the Gran Sasso National Laboratory. *Phys. Rev. Lett.*, 100:021303, 2008.
- [11] T. Bruch et al. Status and future of the CDMS experiment: CDMS-II to SuperCDMS. *AIP Conf. Proc.*, 957:193–196, 2007.
- [12] K. J. Clark. *A new and improved spin-dependent dark matter exclusion limit using the PICASSO experiment*. PhD thesis, Queen’s University, July 2008.
- [13] M. S. Armel-Funkhouser et al. Exclusion limits on the WIMP nucleon cross-section from the first run of the Cryogenic Dark Matter Search in the Soudan underground lab. *Phys. Rev.*, D72:052009, 2005.
- [14] Z. Ahmed et al. A search for WIMPs with the first five-tower data from CDMS. *astro-ph/0802.3530*, 2008.
- [15] Peter F Sorensen. *A position-sensitive liquid xenon time-projection chamber for direct detection of dark matter: The XENON10 Experiment*. PhD thesis, Brown University, July 2008.
- [16] M. Barnabe-Heider et al. Response of superheated droplet detectors of the PICASSO dark matter search experiment. *Nucl. Instrum. Meth.*, A555:184–204, 2005.

- [17] T. Doke, A. Hitachi, J. Kukuchi, K. Matsuda, H. Okada, and E. Shibamura. Absolute scintillation yields in liquid argon and xenon for various particles. *Jpn. J. Appl. Phys*, 41:1538–1545, Mar 2002.
- [18] C. Amsler et al. Luminescence quenching of the triplet excimer state by air traces in gaseous argon. *physics.ins-det*, 2007.
- [19] S. Kubota, A. Nakamoto, T. Takahashi, T. Hamada, E. Shibamura, M. Miyajima, K. Masuda, and T. Doke. Recombination luminescence in liquid argon and in liquid xenon. *Phys. Rev. B*, 17(6):2762–2765, Mar 1978.
- [20] A. Hitachi et al. Effect of ionization density on the time dependence of luminescence from liquid argon and xenon. *Phys. Rev.*, B27:5279–5285, 1983.
- [21] M.G. Boulay and A. Hime. Technique for direction detection of weakly interacting massive particles using scintillation time discrimination in liquid argon. *Astroparticle Physics*, 25, 2006.
- [22] M. G. Boulay. Introduction (DEAP-1 and meeting goals). DEAP-1 analysis meeting at Queen’s University, 2008.
- [23] J. J. Lidgard. Pulse shape discrimination studies in liquid argon for the DEAP-1 detector. Master’s thesis, Queen’s University, April 2008.
- [24] SAES Getters. SAES Getters - MonoTorr PS4 Series. <http://www.saespuregas.com/default.aspx?idPage=1113>, July 2008.
- [25] M.G. Boulay, B. Cai, and the DEAP/CLEAN collaboration. Dark Matter Search at SNOLAB with DEAP-1 and DEAP/CLEAN-3600. Poster for Neutrino 2008 in New Zealand.

- [26] P. Benetti et al. Measurement of the specific activity of Ar-39 in natural argon. *Nucl. Instrum. Meth.*, A574:83–88, 2007.
- [27] A.R. Brosi, H. Zeldes, and B.H. Ketelle. Argon³⁹ Beta-Spectrum. *Phys. Rev.*, 79:902–902, 1950.
- [28] C. Galbiati and R. Purtschert. Discovery of underground argon with low level of radioactive ³⁹Ar and possible applications to WIMP dark matter detectors. *J. Phys. Conf. Ser.*, 120:042015, 2008.
- [29] M. G. Boulay. Neutron and gamma ray backgrounds in DEAP-1 (preliminary), September 2006.
- [30] M. G. Boulay. DEAP-3 NSERC Proposal 327126.
- [31] D. Mei and A. Hime. Muon-induced background study for underground laboratories. *Phys. Rev.*, D73:053004, 2006.
- [32] S. Berko and J. C. Erskine. Angular distribution of annihilation radiation from plastically deformed aluminum. *Physical Review Letters*, 19(6), August 1967.
- [33] P. Hautojärvi. Binding Between Positron and Dislocation in Aluminum. *Solid State Communications*, 11, 1972.
- [34] John Allison et al. GEANT4 developments and applications. *IEEE Trans. Nucl. Sci.*, 53:270, 2006.
- [35] V. A. Kudryavtsev, N. J. C. Spooner, and J. E. McMillan. Simulations of muon-induced neutron flux at large depths underground. *Nucl. Instrum. Meth.*, A505:688–698, 2003.

- [36] NIST. XCOM: Photon cross section data. <http://physics.nist.gov/cgi-bin/Xcom/>, June 2008.
- [37] C. G. Lambe. *Statistical methods and formulae*. The English Universities Press LTD, 1967.
- [38] Bei Cai. DEAP-1 internal document., 2008.

Appendix A

List of runs use in the thesis.

A.1 Runs conducted at Queen's University

Runs conducted at Queen's University. The data were taken with 1 ns time bin and 50 mV/division:

Table A.1: ^{22}Na PSD data with 1 ns time bin and 50 mV/division

Runs	Entries	Trigger (Hz)	Livetime (s)
411	1246800	34.1	36563.05
412	115800	35.0	3308.57
413	421800	33.8	12479.29
414	2074600	38.0	54594.74
415	3878600	39.1	99196.93
416	395100	39.7	9952.14
420	1523900	37.1	41075.47
421	646300	36.5	17706.85
422	1764800	37.1	47568.73
427	1764600	36.6	48213.11
428	631000	36.3	17382.92
429	1476400	35.5	41588.73
430	416600	36.8	11320.65
490	175700	50.1	3506.99
491	2271500	49.9	45521.04
492	1014900	50.2	20217.13
493	1989600	50.5	39398.02
494	694400	51.2	13562.50
496	132000	49.8	2650.60
497	2422800	51.4	47136.19
498	76200	52.6	1448.67
521	336000	51.1	6575.34
522	4402200	51.1	86148.73
523	8389500	52.9	158591.68
525	7891900	51.7	152647.97
528	8585100	51.8	165735.52
529	3802400	50.1	75896.21
532	3907200	51.3	76163.74
533	3232700	51.1	63262.23

Table A.2: ^{22}Na energy calibration

Runs	Entries	Trigger (Hz)	Livetime (s)
419	182000	153.0	1189.54
426	170700	154.6	1104.14
445	2427670	205.0	11842.29
473	264000	205.9	1282.18
495	279600	221.6	1261.73
501	71900	224.7	319.97
513	208600	223.4	933.96
518	618700	222.6	2779.55
524	392400	220.5	1779.91
527	589200	220.8	2668.84
531	234500	218.3	1074.36

Table A.3: Neutron run

Runs	High F_{prompt} events in ROI	Entries	Trigger (Hz)
316	3833	4806500	400

Table A.4: Standard trigger without a source for a muon study

Runs	High F_{prompt} events in ROI	Entries	Trigger (Hz)	Date
393–395	9	6400	0.2	04/09/2007

Table A.5: Background runs on surface at Queen's University

Runs	High F_{prompt} events in ROI	Entries	Trigger (Hz)	Date
436	104	4815200	213.0	15/09/07
437	40	2530099	214.5	16/09/07
438	13	810100	213.9	17/09/07
476	82	3124400	187.4	25/09/07
479	146	5573800	182.7	26/09/07
480	9	419700	178.9	27/09/07
482	106	4921400	222.5	28/09/07
486	141	5418100	182.1	29/09/07
488	132	4326600	165.5	01/10/07
489	27	960600	167.3	01/10/07

A.2 Runs conducted at SNOLAB

The following sets of runs were conducted at SNOLAB and were used as part of the analysis.

Table A.6: ^{22}Na PSD data with 10 ns time bin and 50 mV/division. All runs before run 1488 use the slow output from the NaI PMT, which has wider timing resolution.

Runs	Live time (s)	PMT trigger (Hz)	Trigger (Hz)
1366–1379	8.90E4	8317.8	707.7
1384–1413	2.73E5	8269.4	694.4
1488–1517	3.18E5	8966.8	641.9
1535–1557	1.99E5	8036.8	583.9
1584–1602	1.76E5	4369.4	565.7

Table A.7: ^{22}Na PSD data with 10 ns time bin and 20 mV/division

Runs	Live time (s)	PMT trigger (Hz)	Trigger (Hz)
1603–1615	9.67E4	4369.7	565.7
1622–1651	N/A	6879.4	N/A

Table A.8: ^{22}Na PSD data with 1 ns time bin and 50 mV/division

Runs	Live time (s)	PMT trigger (Hz)	Trigger (Hz)
1726–1728	5.65E2	8916.8	1058.2

Table A.9: ^{22}Na PSD data with 2 ns time bin and 50 mV/division

Runs	Live time (s)	PMT trigger (Hz)	Trigger (Hz)
1737–1741	1.49E4	8916.8	561.6
1780–1796	4.14E4	8116.0	639.5
1799–1817	7.19E4	5842.2	514.8
1883–1888	N/A	N/A	N/A

Table A.10: Runs used in the pile up study. 1711 is a run with SNO AmBe neutron source. 1720–1725 is a set of runs with both SNO AmBe neutron source and ^{22}Na γ s source.

Runs	Live time (s)	PMT trigger (Hz)	Trigger (Hz)
1711	1.71E3	N/A	279.4
1720–1725	2.70E4	8881.6	1047.8

Table A.11: ^{22}Na energy calibration with with 10 ns time bin and 50 mV/division

Runs	Live time (s)	PMT trigger (Hz)	Trigger (Hz)
1523	2.0E3	7830.8	1074.7

Table A.12: ^{22}Na a full spectrum DEAP–1 trigger

Runs	Live time (s)	PMT trigger (Hz)	Trigger (Hz)
1839	7.3E1	N/A	9768.8

Table A.13: Background with 1 ns time bin and 50 mV/division setting

Runs	Live time (s)	Trigger (Hz)	Starting Date
1751–1774	4.1E4	155.1	14/10/08
1826–1833	2.7E4	157.0	21/10/08
1865–1869	3.1E4	152.5	27/10/08

Table A.14: Background with 10 ns time bin and 50 mV/division setting

Runs	Live time (s)	Trigger (Hz)	Starting Date
1570–1582	1.43E5	153.0	10/09/08